



Catalytic consequences of reactive oxygen species during C₃H₆ oxidation on Ag clusters



Petar T. Lachkov, Ya-Huei (Cathy) Chin*

Department of Chemical Engineering and Applied Chemistry, University of Toronto, Toronto, Canada

ARTICLE INFO

Article history:

Received 7 June 2018

Accepted 5 July 2018

Available online 20 August 2018

Keywords:

Propylene

Propylene oxide

Epoxidation

Alkene oxidation

Combustion

Chemisorbed oxygen

Ag cluster

Hydroperoxyl species

Hydrogen abstraction

Oxygen coverage

ABSTRACT

Rate measurements in the kinetically controlled regime, kinetic fittings, and isothermal C₃H₆ and O₂ uptake experiments lead to a proposed mechanism for C₃H₆ epoxidation and combustion reactions on predominantly O* covered Ag cluster surfaces. Epoxidation occurs via kinetically relevant reactions between chemisorbed oxygen adatoms (O*) and gas phase C₃H₆. In contrast, combustion occurs via kinetically relevant hydroperoxyl (OOH*) formation, formed from H transfer from H₂O* to O₂. C₃H₆ oxidation reactions with C₃H₆-O₂-H₂O-H₂O₂ mixtures show that H₂O₂ derived OOH* species are more effective oxidants than O* for C₃H₆ combustion, as confirmed from H₂O₂/D₂O₂ kinetic isotope effects. Both C₃H₆* and O* coverages are near or at chemical equilibrium during steady-state reactions, as confirmed from in-situ chemical titrations. C₃H₆O and CO_x site-time-yields and CO_x selectivities increase with increasing Ag cluster diameters and Ag surface coordination, because O*, O₂*, H₂O*, and OOH* oxidants remain more weakly bound and therefore much more reactive.

© 2018 Elsevier Inc. All rights reserved.

1. Introduction

Propylene (C₃H₆) epoxidation reactions produce propylene oxide (C₃H₆O), an important precursor for the synthesis of polymers, antifreezes, and solvents [1–3]. Conventional propylene epoxidation processes use chlorine and calcium hydroxide [3,4], alkyl hydroperoxides {(CH₃)₃COOH, C₆H₅CH(CH₃)OOH, or C₆H₅C(CH₃)₂OOH} [3,5,6], hydrogen peroxide [2,3], or hydrogen-oxygen mixtures [2,7–9] as the co-reagents. These reagents are expensive and their use leads to either chemical waste or generation of co-products at stoichiometric ratios [1–3]. The H₂O₂ and H₂-O₂ epoxidation processes are practical pathways and remain superior alternatives for modern plants [1]. However, a direct epoxidation route that inserts an oxygen atom from a molecular O₂ into the C=C bond of C₃H₆ is an attractive route, if one could minimize CO_x formation. If carried out selectively, this route produces only C₃H₆O.

Direct epoxidation with O₂ is the preferential pathway for ethylene oxide (C₂H₄O) formation from ethylene (C₂H₄) on Ag catalysts [1,2,10–12]. In contrast, C₃H₆ epoxidation with molecular O₂ remains unselective on Ag catalysts with much lower yields, when

comparing at similar conditions. At moderate temperatures and identical conditions, C₃H₆ epoxidation rates are lower than C₂H₄ epoxidation rates, i.e., 4–10 times smaller on 49–656 nm Ag clusters (O₂/C_nH_{2n} = 2, n = 2 or 3, 473 K) [13] and 45 times smaller on polycrystalline Ag (O₂/C_nH_{2n} = 3.3, 440 K) [14]. Fig. 1a and 1b summarize the Arrhenius relation for the first-order rate coefficients ($k_i = r_i[C_nH_{2n}]^{-1}$, where r_i is the site-time-yield of species i , $i = C_nH_{2n}O$ or CO_x) for C_nH_{2n} epoxidation and combustion, respectively, on Ag based catalysts reported in the literature [13–18]. At similar reaction conditions, the $k_{C_3H_6O}$ values are between zero and two orders of magnitude smaller than the $k_{C_2H_4O}$ values (Fig. 1a), indicating that epoxidation occurs less effectively for C₃H₆ than C₂H₄.

Kinetic [14,18–20] and surface science [12,18,19,21] studies have disagreed on whether C₂H₄ and C₃H₆ epoxidation occur via atomic [19,21] or molecular [12,14,18] oxygen insertion. Kinetic studies [10,11,22] and density functional theory (DFT) calculations [10,23] proposed that a chemisorbed oxygen adatom (O*, where * denotes a Ag site) inserts into C₂H₄, forming an oxametallacycle (Ag-O-CH₂-CH₂-Ag) intermediate [11,23] during C₂H₄-O₂ reactions, as detected with high resolution electron energy loss spectroscopy (HREELS) during C₂H₄O adsorption on Ag(111) at 250 K and calculated with DFT [23]. Similarly, C₃H₆-O₂ reactions also occur via the same route that involves oxametallacycle intermediates [24–27]. In contrast, the alternative mechanistic proposal suggested that

* Corresponding author.

E-mail address: cathy.chin@utoronto.ca (Y.-H. (Cathy). Chin).

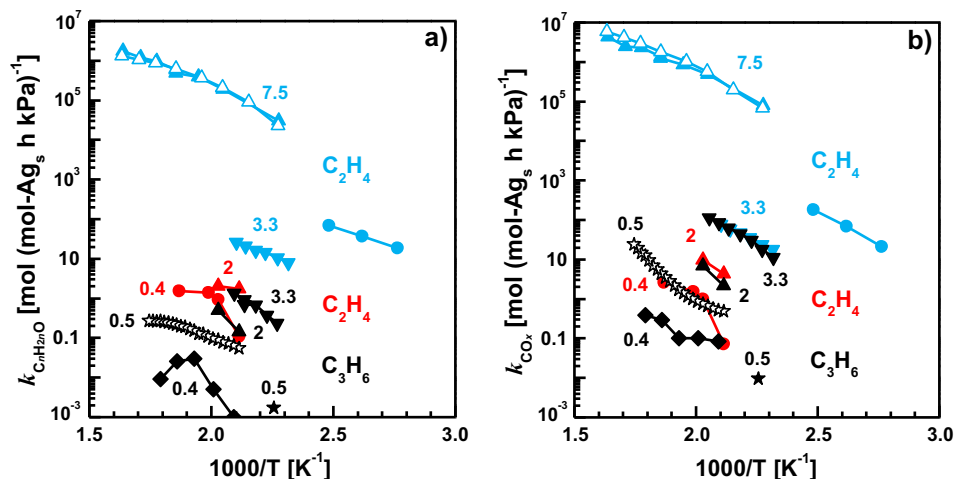


Fig. 1. First-order rate coefficients ($k_i = r_i/[C_nH_{2n}]^{-1}$, where r_i is the site-time-yield of species i : $C_nH_{2n}O$ or CO_x , $n = 2$ or 3) of C_2H_4 (▲, ●, △, ◆, ▼) and C_3H_6 (★, ☆, ◆, ▲, ▼) (a) epoxidation and (b) combustion during C_2H_4 - O_2 and C_3H_6 - O_2 reactions on 1 and 5 wt% Ag/SiO₂ (3.1 nm clusters pre-treated with 3 kPa O₂ and 6 kPa C₃H₆ at 573 K: ☆, 5.1 nm clusters pre-treated with 3 kPa O₂ and 6 kPa C₃H₆ at 443 K: ★, this work), 20 wt% Ag 0.1 wt% Y₂O₃ 0.1 wt% K₂O/Al₂O₃ (◆, 16 nm clusters) [16], 7 wt% Ag/CaCO₃ (▲, ●, 149 nm clusters) [13], 1.71 wt% Ag/SiO₂ (●, 13 nm clusters) [17], Ag(1 1 0) (△) [18], Ag(1 1 1) (▲) [18], and polycrystalline Ag (▼ and ▼) [14]; (●) [15]) plotted against the inverse temperature. The O₂/C_nH_{2n} feed ratios during the rate measurements are denoted in the figure.

O₂* reacts directly with C₂H₄ [12,14,18] or C₃H₆ [14], cleaving its O=O bond and forming C_nH_{2n}O* and O*.

In parallel to epoxidation reactions, olefins also undergo combustion with O₂ on Ag catalysts [1,2,10–12]. At identical conditions, the combustion rates for C₃H₆ are smaller than C₂H₄: ~1.2 times smaller on Ag/CaCO₃ (O₂/C_nH_{2n} = 2, 473 K) [13] and two times smaller on polycrystalline Ag (O₂/C_nH_{2n} = 3.3, 440 K) [14]. Likewise, the k_{CO_x} values are similar for C₃H₆ and C₂H₄ combustion (Fig. 1b). These findings contradict the expected marked increase in the hydrocarbon combustion rate with increasing carbon number and with the concomitant decrease in C–C and C–H bond strengths [28,29]. Kinetic [14,18,19] and surface science [12,18,19,21] studies have not led to an unambiguous conclusion on the catalytic involvement of either molecular oxygen [14,18] or atomic oxygen [12,19,21] in C₂H₄ and C₃H₆ combustion. In the molecular pathway, the adsorbed O₂* initiates C₃H₆ combustion by abstracting the γ -H [14]. DFT calculations on Ag(1 0 0), Ag(1 1 1), as well as Ag₁₉ clusters supported on Al₂O₃ [24–27] have proposed, however, that the oxygen adatom instead of molecular oxygen is the γ -H abstractor that leads to allyl (C₃H₅*) formation as the intermediate in C₃H₆ combustion.

Others have examined the C₃H₆-O₂ reactivity trends on supported Ag [13,26,30], Cu [30,31], Au [30,32,33], bimetallic Ag-Cu [34], Group 4–12 metal oxide [35], as well as Ag and Cu based materials promoted with K₂O [16,36], BaO [16], CaO [16], and Y₂O₃ [16]. Despite these studies, the kinetic dependencies for the individual epoxidation and combustion reactions and the mechanistic reason behind the poor selectivity for C₃H₆ epoxidation on Ag clusters have not yet been resolved completely [37]. With this in mind, the objective of this study is to understand mechanistically what leads to the poor selectivity in C₃H₆ epoxidation. Here, we probe the rate dependencies, identity of the most abundant surface intermediates, and the reactive oxygen species with combined kinetic, isotopic, and chemical titration methods on Ag clusters dispersed on inert SiO₂ supports. We interpret the kinetic dependencies for these concomitant reactions in the kinetically controlled regime by considering the involvements of the various oxygen species derived from O₂ and H₂O, where the latter is a by-product from the undesired combustion reaction. H₂O plays a significant role in C₃H₆ oxidation, possibly because its reaction with a diatomic oxygen (O₂*) forms a hydroperoxyl intermediate (OOH*) that participates in the combustion reaction, as confirmed

from strong H₂O₂/D₂O₂ kinetic isotope effects. We show that O* and C₃H₆* co-exist on Ag cluster surfaces during C₃H₆-O₂ reactions. Larger Ag clusters, due to their weaker binding to adsorbed species, are more reactive for both the epoxidation and combustion reactions. These larger clusters, however, promote the combustion reaction to a larger extent, leading to lower epoxidation selectivities.

2. Catalyst preparation and experimental methods

2.1. Synthesis of supported Ag clusters dispersed on porous SiO₂ particles

Supported silver catalysts were prepared by the incipient wetness impregnation method. Silica (Grace, Davisil Chromatographic Silica, 1.23 cm³ g⁻¹ pore volume, 15 nm pore diameter, 330 m² g⁻¹, 70–200 μ m SiO₂ diameter) was crushed to <75 μ m particle diameter (defined as the support diameter). The silica particles were heated at 0.033 K s⁻¹ in stagnant ambient air and were held at 673 K for 4 h and then cooled to 393 K. The treated silica particles were impregnated with an aqueous silver nitrate solution, which was prepared by dissolving AgNO₃ (Sigma-Aldrich, 99.9999% trace metal basis) in doubly deionized water (>18.2 M Ω cm), to achieve a silver loading of 1 or 5 wt%. The sample was next dried for 24 h at 353 K in stagnant ambient air prior to treatment in flowing dry air (Linde, 99.99%) at 0.5 cm³ STP g⁻¹ s⁻¹ by heating at 0.033 K s⁻¹ to 773 K and holding for 2 h, before cooling to ambient temperature and introducing flowing He (Linde, 99.999%) at 0.5 cm³ STP g⁻¹ s⁻¹ for 0.5 h. The sample was heated at 0.033 K s⁻¹ in 0.5 cm³ STP g⁻¹ s⁻¹ flowing H₂ (Linde certified standard, 5% H₂ in He) to 598–723 K for 5 h to achieve Ag clusters with a range of mean diameters. Ag clusters with 3.1 and 11.3 nm diameters were produced from 1 wt% Ag/SiO₂ catalysts treated in H₂ at 598 and 723 K, respectively, while 5.1 and 29.3 nm Ag clusters were produced from 5 wt% Ag/SiO₂ catalysts treated in H₂ at 598 and 723 K, respectively. After the treatment, the sample was cooled under flowing He at 0.5 cm³ STP g⁻¹ s⁻¹. At ambient temperature, a flowing 1% O₂–4% N₂–95% He stream {prepared from air (Linde, 99.99%) and He (Linde, 99.999%); 0.5 cm³ STP g⁻¹ s⁻¹} was introduced to the catalyst for 6 h. Ag/SiO₂ powders were mixed with SiO₂ at SiO₂-to-catalyst mass ratios of 1 and 3. Undiluted and diluted 1 and 5 wt% Ag/SiO₂ powders were pressed

into pellets using a pellet die (Carver, 31 mm ID) at 130 MPa for 0.5 h in a hydraulic press (Specac). The resulting disc was then crushed and sieved to obtain particles between 125 μm and 180 μm .

2.2. Isothermal volumetric O_2 , H_2 , and C_3H_6 uptake measurements

O_2 (Linde, 99.995%), H_2 (Linde, 99.999%), and C_3H_6 (Linde, 99.95%) uptakes were carried out at 443 K using a volumetric adsorption-desorption apparatus (10.6 cm^3_{STP} gas manifold and 11.4 cm^3_{STP} reaction chamber) connected to a pressure transducer (MKS, 120AA Baratron, dual ranges of 0–13 and 0–133 kPa, 0.1% accuracy), vacuum turbopump (Pfeiffer, HiPace 80), diaphragm pump (Pfeiffer, MVP 015-2), 6-way valve (Valco Instruments, H-EHC6WEZ), and thermal mass flow controllers (Brooks, SLA5850). The total leak rate of the system was $5 \times 10^{-8} \text{ cm}^3_{\text{STP}} \text{ h}^{-1}$ at 443 K. Catalysts were loaded into a quartz sample holder and heated under flowing H_2 (Linde, 99.999%, $0.5 \text{ cm}^3_{\text{STP}} \text{ g}^{-1} \text{ s}^{-1}$) at 0.033 K s^{-1} to 598 K, where they were held for 1 h. The sample holder and manifold were evacuated under dynamic vacuum (10^{-5} Pa) for at least 12 h at 598 K before being cooled to 443 K. The mean Ag cluster diameter was determined from the difference between the total and reversible extrapolated O_2 uptakes at 443 K at zero O_2 pressure [38], a surface O-to-surface Ag atomic ratio of unity ($\text{O}_s/\text{Ag}_s = 1$, subscript s denotes surface atoms) [39,40], and an assumption of hemispherical Ag clusters with a density similar to bulk Ag (10.49 g cm^{-3}) [41].

O^* coverages during steady-state $\text{C}_3\text{H}_6\text{-O}_2$ reactions were quantified by O_2 chemical titrations, carried out in-situ with the same volumetric adsorption-desorption apparatus using methods described above, after treating the spent catalyst in flowing He (Linde, 99.999%, $0.5 \text{ cm}^3_{\text{STP}} \text{ g}^{-1} \text{ s}^{-1}$) for 0.5 h and evacuating the reactor for 0.5 h at 443 K. The difference between the total and reversible O_2 uptakes, extrapolated to zero O_2 pressure $\{(\text{O}_s/\text{Ag}_s)_{\text{uptake}}\}$, was subtracted from unity to obtain the O^* coverage during steady-state $\text{C}_3\text{H}_6\text{-O}_2$ reactions $\{(\text{O}_s/\text{Ag}_s)_{\text{SS}}\}$, subscript SS denotes steady-state, see details in Section S7.

2.3. Rate and selectivity assessments for oxidation reactions on Ag clusters

Rates and selectivities (defined as the percentage of C in a specific product species relative to the total amount of C in all products) of $\text{C}_3\text{H}_6\text{-O}_2$, $\text{C}_3\text{H}_6\text{-O}_2\text{-H}_m\text{D}_{2-m}\text{O}$, and $\text{C}_3\text{H}_6\text{-O}_2\text{-H}_m\text{D}_{2-m}\text{O-H}_p\text{D}_{2-p}\text{O}_2$ ($m, p = 0, 1, \text{ or } 2$) reactions were measured in a fixed bed microcatalytic quartz reactor (8.1 mm ID) operating at differential conversions. Catalyst particles (125–180 μm) were supported on a quartz frit inside the tubular reactor, which was placed in a resistively heated furnace (Bluewater Heater) equipped with a K-type thermocouple (Omega) in contact with the catalyst bed. The sample was pretreated with $0.5 \text{ cm}^3_{\text{STP}} \text{ g}^{-1} \text{ s}^{-1}$ H_2 (Linde, 99.999%) by heating at 0.033 K s^{-1} to 598 K and holding for 1 h. He (Linde, 99.999%) was subsequently introduced at $0.5 \text{ cm}^3_{\text{STP}} \text{ g}^{-1} \text{ s}^{-1}$ for 0.5 h before cooling to the reaction temperature (323–573 K). Reactant gas mixtures of O_2 (Linde certified standard, 5% O_2 in He), C_3H_6 (Linde, 99.95%), and balance He (Linde, 99.999%) were prepared by metering the individual gas flow rates independently with thermal mass flow controllers (Brooks, SLA5850). In selected experiments, liquid H_2O (doubly deionized, $>18.2 \text{ M}\Omega \text{ cm}$) or H_2O_2 (Sigma-Aldrich, 30 wt% in H_2O) was introduced through a syringe (Scientific Glass Engineering, 0.25 mL) mounted on a syringe infusion pump (KD Scientific, KDS100) into a vaporizing zone held isothermally at 323 K, located upstream from the reactor. All gas transfer lines were held at 323 K such that $\text{H}_m\text{D}_{2-m}\text{O}$ ($<1.1 \text{ kPa}$) and $\text{H}_p\text{D}_{2-p}\text{O}_2$ ($<0.25 \text{ kPa}$) remained in the vapor phase. The chemical compositions of the reactor effluent stream were determined with a gas chromatograph (SRI, 8610C) equipped with molecular sieve 13X

(SRI, $6' \times 1/8''$ SS) and HayeSep D (SRI, $6' \times 1/8''$ SS) packed columns installed in series (with an optional bypass around the 13X column) leading to a thermal conductivity detector (TCD), a micro-methanizer, and then a flame ionization detector (FID) connected in series.

The reactions were carried out at atmospheric pressure and a space velocity of $2 \times 10^3 \text{ cm}^3_{\text{STP}} \text{ g}_{\text{cat}}^{-1} \text{ h}^{-1}$ (on 0.5 g_{cat}) for 8 h at reference conditions (0.25 kPa O_2 and between 6 and 50 kPa C_3H_6 for $\text{C}_3\text{H}_6\text{-O}_2$ reactions; 0.25 kPa O_2 , 50 kPa C_3H_6 , and 1.1 kPa H_2O for $\text{C}_3\text{H}_6\text{-O}_2\text{-H}_2\text{O}$ reactions; 0.25 kPa O_2 , 50 kPa C_3H_6 , 1.1 kPa $\text{H}_m\text{D}_{2-m}\text{O}$, and 0.15–0.25 kPa $\text{H}_p\text{D}_{2-p}\text{O}_2$ for $\text{C}_3\text{H}_6\text{-O}_2\text{-H}_m\text{D}_{2-m}\text{O-H}_p\text{D}_{2-p}\text{O}_2$ reactions, balance He). After this period, the reactant and product concentrations in the effluent streams were not affected by the time-on-stream (less than 5% changes over the final 2 h). Next, partial pressures of the reactants were varied systematically over the entire pressure range (0.25–5.17 kPa O_2 , 2–50 kPa C_3H_6 , 0–1.1 kPa $\text{H}_m\text{D}_{2-m}\text{O}$, 0–0.25 kPa $\text{H}_p\text{D}_{2-p}\text{O}_2$, balance He) in 0.5 h intervals. The reactivity remained stable, because rates decreased by less than 10% at the reference reaction conditions over the entire length of the kinetic studies (8–16 h).

Rates and selectivities of $\text{C}_3\text{H}_6\text{O-O}_2$ (acetone and propylene oxide) and $\text{CH}_3\text{OH-O}_2$ reactions were measured with the same reactor system described above. Acetone (Sigma-Aldrich, 99.9%) and propylene oxide (Sigma-Aldrich, 99.5%) were introduced into the reactant gas mixture using a He bubbler immersed in a dry ice and isopropanol (Sigma Aldrich, 99.7%) bath at 195 K. The bubbler effluent was mixed with a mixture of O_2 and He to attain the desired $\text{C}_3\text{H}_6\text{O}$ (acetone or propylene oxide)- $\text{O}_2\text{-He}$ feed mixtures. $\text{CH}_3\text{OH-O}_2$ reaction mixtures were prepared by introducing liquid CH_3OH (Sigma-Aldrich, 99.8%) through a syringe (Scientific Glass Engineering, 5 mL) mounted on a syringe infusion pump (KD Scientific, KDS100) into a vaporizing zone held isothermally at 353 K, where it was evaporated and mixed with the flowing O_2 and He stream. All gas transfer lines were held at 353 K throughout the $\text{CH}_3\text{OH-O}_2$ rate assessments to prevent the condensation of reactants and products.

3. Results and discussion

3.1. Equilibrium O_2 and C_3H_6 coverages on Ag/SiO_2 catalysts under conditions relevant for C_3H_6 epoxidation catalysis

Oxygen uptakes on Ag clusters at 443 K give monolayer O_t/Ag_t ratios (subscript t denotes total number of Ag atoms), as established previously [39,40,42], by comparing with N_2 or N_2O uptakes and with cluster diameters derived from X-ray line broadening and electron microscopy. Fig. 2 shows the irreversible oxygen uptakes, in terms of O_t/Ag_t ratios, as a function of O_2 pressure for a series of 1 and 5 wt% Ag/SiO_2 samples at 443 K. Extrapolation of these O_t/Ag_t ratios to zero O_2 pressure gives the $(\text{O}_t/\text{Ag}_t)_{0 \text{ kPa}}$ ratio that defines the monolayer coverage ($\text{O}_s/\text{Ag}_s = 1$). This method gives 3.1, 5.1, 11.3, and 29.3 nm average Ag cluster diameters for the series of catalysts.

Fig. 3a shows the total O_t -to-surface Ag_s ratios (O_t/Ag_s) on 5.1 nm Ag clusters (5 wt% Ag/SiO_2) at 443 K. The O_t/Ag_s ratio increases from 0.16 and reaches values above 0.9 at 2 kPa. Assuming Langmuirian surfaces, these data points give the equilibrium constant for O_2 dissociative adsorption, which forms oxygen adatoms (O^* ; $K_{\text{O}_2, \text{dissociation}} = K_{\text{O}_2} K_{\text{O}}$, where K_{O_2} and K_{O} are the equilibrium constants for Steps 1 and 2, respectively, in Scheme 1), of $26 \pm 1 \text{ kPa}^{-1}$. This value, together with the entropy loss ($\Delta S_{\text{ads}, \text{O}^*}$, per oxygen adatom) of $-91 \text{ J (mol O)}^{-1} \text{ K}^{-1}$, estimated by assuming the complete loss of translational and rotational degrees of freedom of $\text{O}_2(\text{g})$ upon its dissociative adsorption, gives the average heat of O_2 dissociative adsorption ($Q_{\text{ads}, \text{O}^*} = -\Delta H_{\text{ads}, \text{O}^*}$, per oxygen

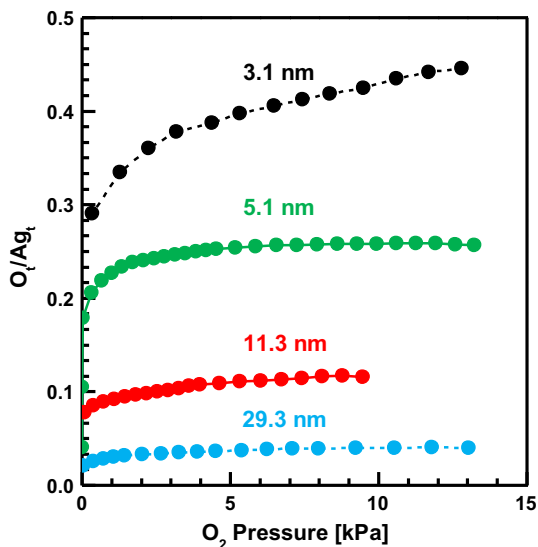


Fig. 2. Equilibrium irreversible O_2 uptakes as the total oxygen-to-total Ag atomic ratio (O_t/Ag_t) on 3.1 (●), 5.1 (●), 11.3 (●), and 29.3 (●) nm Ag clusters (1 and 5 wt% Ag/SiO₂) at 443 K as a function of O_2 pressure (0.08–1 h dwell time).

adatom) of 55 ± 1 kJ (mol O)⁻¹ (calculations in Section S2). This heat of atomic O* adsorption on 5.1 nm Ag clusters is slightly larger than the previously measured values of 33–52 kJ (mol O)⁻¹ on polycrystalline Ag [40,43], apparently because Ag clusters contain a larger fraction of coordinatively unsaturated corner and edge sites, which bind to O* more strongly than the terrace sites prevalent on the bulk Ag structures.

Fig. 3b shows the C₃H₆ uptake isotherm, which includes the weakly adsorbed C₃H₆* species, expressed in terms of the total C₃H₆-to-surface Ag ratio (C₃H_{6,t}/Ag_s) on the same catalyst (5.1 nm Ag) at 443 K. As the C₃H₆ pressure increases from 0.18 to 42 kPa, the C₃H₆* uptakes increase less than linearly from 0.005 to 0.19 ML. Both the α and β carbons of adsorbed C₃H₆ interact with a Ag atom through the C₃H₆ π orbital centered above a single Ag site [44]. The concentration of sites occupied by C₃H₆, [C₃H₆*], relates directly to C₃H₆ pressure and the concentration of uncovered Ag sites ([*]) via:

$$[C_3H_6^*] = K_{C_3H_6}[C_3H_6]^\gamma [*] \quad (1)$$

where $K_{C_3H_6}$ is the equilibrium constant of C₃H₆ adsorption (Step 6, Scheme 1); γ is a parameter capturing the adsorption behavior with its value equal to unity for Langmuirian surfaces [45]. A Langmuirian treatment of the C₃H₆ uptakes results in a poor correlation between the measured and calculated C₃H₆* coverages (regression results in Section S3), likely due to the large C₃H₆* footprint that causes repulsion between the C₃H₆* adsorbates. A treatment of these uptakes with Temkin isotherm [46], which assumes that the heat of C₃H₆ adsorption ($\Delta Q_{ads,C_3H_6}$) decreases linearly with C₃H₆* coverage, also does not capture the measured uptakes (in Section S3), simply because the heat of C₃H₆ adsorption does not vary linearly with C₃H₆* coverage. We utilize the Sips isotherm [47], which accounts for both the difference in heats of adsorption and the change in adsorbate coverages. This treatment assumes that the heats of C₃H₆* adsorption follow an exponential distribution; it is a variation of the Freundlich isotherm that sets the total number of available sites constant [47]. The Sips isotherm sets the coefficient γ in Eq. (1) between 0 and 1 and uses this coefficient to describe these distributions. Non-linear regression of Eq. (1) as the objective function against the C₃H₆ uptakes (Fig. 3b) provides the $K_{C_3H_6}$ and γ coefficient values of 0.012 ± 0.01 kPa^{-0.78} and 0.78, respectively, at the coverages and temperature relevant for C₃H₆ epoxidation catalysis. The calculated γ value (0.78) is smaller than unity, due to strong adsorbate-adsorbate interactions among the C₃H₆* surface species, even at the low coverages (0.005 and 0.19 ML). Fig. 3b also includes the predicted C₃H_{6,t}/Ag_s ratios from the Sips adsorption model.

3.2. Kinetic dependencies for C₃H₆ epoxidation and combustion on dispersed Ag clusters

C₃H₆ and O₂ reactions on Ag/SiO₂ catalysts form C₃H₆O, the desired product, as well as side products CO_x (x = 1 or 2) and H₂O over a wide range of reactant pressures and temperatures (2–50 kPa C₃H₆, 0.25–5.17 kPa O₂, 323–573 K, 2×10^3 cm³_{STP} g_{cat}⁻¹ h⁻¹). The reactions may also form acrolein, propanal, and acetone, as reported previously on Ag/SiO₂ (573 K) [48], Ag/Al₂O₃ promoted with Y₂O₃ (518 K) [16], Ag-Ir/CaCO₃ (533 K) [49], and Ag-Rh/CaCO₃ (533 K) [49] catalysts. These intermediates, however, remain undetected in this work within the experimentally measurable limits (0.1 ppmv,

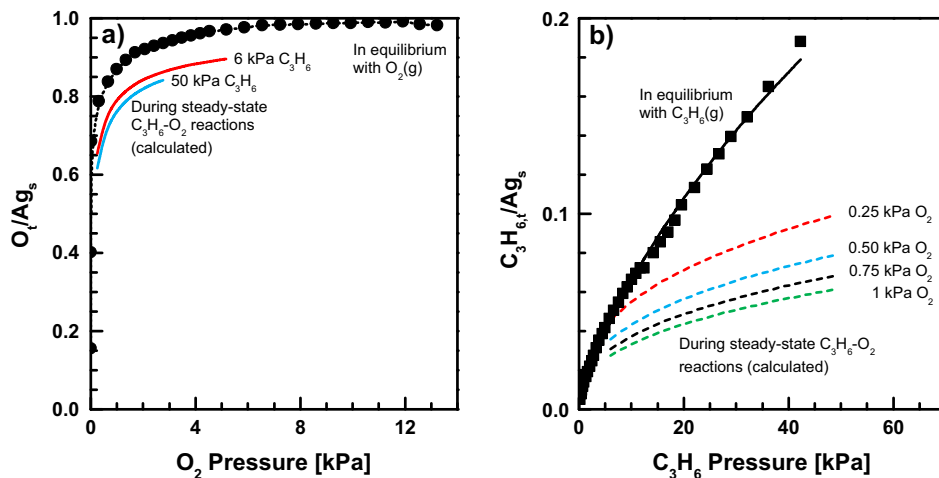


Fig. 3. (a) Equilibrium O* uptakes (O_t/Ag_s) measured by O_2 titration (●) and steady-state O* coverages during C₃H₆-O₂ reactions on Ag catalysts (5 wt% Ag/SiO₂, 5.1 nm clusters), calculated from Eq. (5) and parameter values in Table 1 at 6 (—) and 50 (—) kPa C₃H₆, plotted as a function of O_2 pressure at 443 K. (b) Equilibrium C₃H₆* uptakes (C₃H_{6,t}/Ag_s) measured by C₃H₆ titration (■) and predicted by the Sips adsorption model (—), and steady-state C₃H₆* coverages during C₃H₆-O₂ reactions on Ag catalysts (5 wt% Ag/SiO₂, 5.1 nm clusters), determined using Eq. (6) and parameter values in Table 1 at 0.25 kPa O₂ (—), 0.5 kPa O₂ (—), 0.75 kPa O₂ (—), and 1 kPa O₂ (—), plotted as a function of C₃H₆ pressure at 443 K.

	Step	Elementary Reaction	Rate or Equilibrium Constant
a	1	$O_2 + * \rightleftharpoons O_2^*$	K_{O_2}
	2	$O_2^* + * \rightleftharpoons 2O^*$	k_{O_2}, k_{O_2}, K_O
b	3	$H_2O + * \rightleftharpoons H_2O^*$	K_{H_2O}
	4	$H_2O^* + O_2^* \xrightarrow{-\Delta} OOH^* + OH^*$	k_{OOH}
	5	$H_2O^* + O^* \rightleftharpoons 2OH^*$	K_{OH}
c	6	$C_3H_6 + * \rightleftharpoons C_3H_6^*$	$K_{C_3H_6}$
	7	$C_3H_6^* + O^* \rightleftharpoons C_3H_6-O^* (OMC) + *$	$K_{C_3H_6-O^*}$
	8	$C_3H_6-O^* (OMC) \xrightarrow{-\Delta} C_3H_6O^* (PO)$	$k_{C_3H_6O^*}$
	9	$C_3H_6O^* (PO) \rightarrow C_3H_6O + *$	$k_{C_3H_6O^*}$
d	10	$C_3H_6^* + O^* \xrightarrow{-\Delta} C_3H_5^* (allyl) + OH^*$	$k_{C_3H_6-O^*}$
	11	$C_3H_6^* + OOH^* \rightarrow C_3H_5^* (allyl) + OOH_2^*$	$k_{C_3H_6-OOH^*}$
	12	$OOH_2^* \rightarrow O^* + H_2O$	k_{OOH_2}
	13	$CO^* \rightleftharpoons CO + *$	K_{CO}
	14	$CO^* + O_2^* \rightarrow CO_2^* + O^*$	k_{CO_2}
	15	$CO_2^* \rightleftharpoons CO_2 + *$	K_{CO_2}

Scheme 1. A proposed sequence of elementary steps during (a) O_2 and (b) H_2O activation, and C_3H_6 (c) epoxidation and (d) combustion reactions on Ag clusters (* denotes a Ag site, \rightarrow denotes an irreversible step, $\xrightarrow{-\Delta}$ a rate determining step, \rightleftharpoons a quasi-equilibrated step, and \rightleftharpoons a reversible step. K_j is the equilibrium constant, k_j or k_{ij} is the forward rate constant, and k_{-j} is the reverse rate constant for the respective elementary reaction. Subscript j denotes the specific reaction.)

which corresponds to a carbon selectivity of 0.01%) under all reaction conditions.

Fig. 1a and 1b compare the temperature effects (362–613 K) on the first-order rate coefficients ($k_i = r_i [C_nH_{2n}]^{-1}$, where r_i is the site-time-yield of species i , $i = C_nH_{2n}O$ or CO_x , $n = 2$ or 3) for C_3H_6 epoxidation and combustion reactions occurring on 3.1 and 5.1 nm Ag clusters with those reported for C_nH_{2n} on supported Ag catalysts [13,16,17], polycrystalline Ag [14,15], and well-defined single crystal Ag surfaces [18]. At similar conditions, the $k_{C_3H_6O}$ (Fig. 1a) and k_{CO_x} (Fig. 1b) values in this work are within one order of magnitude of other literature measurements.

Fig. 4a and 4b show the C_3H_6O and CO_x site-time-yields ($r_{C_3H_6O}$ and r_{CO_x}), respectively, as a function of O_2 pressure (0.25–5.17 kPa), for constant C_3H_6 pressures on 5.1 nm Ag clusters (5 wt% Ag/SiO₂) at 443 K. The selectivities towards C_3H_6O are highest (80%) at the lowest O_2 (0.25 kPa) and largest C_3H_6 (50 kPa) pressures, but their values decrease to 28% as the O_2 pressure increases (to 5.17 kPa) and the C_3H_6 pressure decreases (to 6 kPa). Over the entire operating O_2 and C_3H_6 pressure ranges, the ratios for CO-to- CO_2 site-time-yields, $r_{CO} (r_{CO_2})^{-1}$, remain constant at 0.20 ± 0.05 . C_3H_6O and CO_x site-time-yields (r_i , $i = C_3H_6O$ or CO_x) vary with O_2 and C_3H_6 pressures (denoted as $[O_2]$ and $[C_3H_6]$), according to:

$$r_i = k_{\text{eff},i} [O_2]^{\alpha_i} [C_3H_6]^{\beta_i} \quad (2)$$

where $k_{\text{eff},i}$ is the effective rate constant, and α_i and β_i are the apparent reaction orders with respect to O_2 and C_3H_6 , respectively, for the site-time-yield of species i .

C_3H_6O site-time-yields (Fig. 4a) from the epoxidation reaction increase much less than linearly with O_2 and become insensitive to O_2 with increasing O_2 pressures. At 6 kPa C_3H_6 , the apparent O_2 order ($\alpha_{C_3H_6O}$) varies from 0.2 ± 0.1 to 0 ± 0.05 . The C_3H_6O site-time-yields also increase less than linearly with C_3H_6 ; here, the reaction order with respect to propylene, $\beta_{C_3H_6O}$, decreases from 0.7 to 0.3 (± 0.1), as the C_3H_6 pressure increases from 6 to 50 kPa. The O_2 dependence is consistent with that reported on polycrystalline Ag, where $\alpha_{C_3H_6O}$ decreases from 1 to 0 as the O_2 pressure

increases from 2.7 to 16 kPa (at 3.7 kPa C_3H_6 , 440 K) [14], but the C_3H_6 dependence deviates from previous results, where the C_3H_6O site-time-yields remain insensitive to C_3H_6 pressure ($\beta_{C_3H_6O} = 0$, 0.8–7 kPa C_3H_6 , 17 kPa O_2 , 431 K) [14].

CO_x site-time-yields (Fig. 4b) from the parallel combustion reactions increase less than linearly with O_2 pressures ($\alpha_{CO_x} = 0.55 \pm 0.05$) and decrease marginally with increasing C_3H_6 pressures ($\beta_{CO_x} = -0.10 \pm 0.05$). These dependencies are similar to those on polycrystalline Ag (431–440 K), on which α_{CO_x} decreases from 1 to 0 while the CO_x site-time-yields remain insensitive to C_3H_6 ($\beta_{C_3H_6O} = 0$) for all C_3H_6 pressures [14]. These different O_2 dependencies between the C_3H_6O and CO_x site-time-yields suggest that either the types of oxidants or the molecularity of oxygen involved in the elementary steps leading to the kinetically relevant step, or both of these items, differ between the reactions that form C_3H_6O and CO_x .

3.3. Proposed elementary steps and rate expressions for C_3H_6 epoxidation and combustion on dispersed Ag clusters

A plausible reaction mechanism for C_3H_6 oxidation must describe both the observed rate dependencies for C_3H_6O and CO_x site-time-yields. In order to connect the O^* coverages to rates, we compare the profiles of O^* coverages at chemical equilibrium (without reactions) and of C_3H_6O and CO_x site-time-yields, measured at the lowest C_3H_6 pressure of 6 kPa, as a function of O_2 pressure in Fig. 4c. The profile of C_3H_6O site-time-yields ($r_{C_3H_6O}$) closely resemble that of equilibrium O^* coverages. At this low C_3H_6 pressure, Ag surfaces are largely free of C_3H_6 derived intermediates (<0.05 ML, Fig. 3b). Both the C_3H_6O site-time-yields and equilibrium O^* coverages initially increase rapidly and then become nearly constant as the O_2 pressure increases. These similar profiles suggest the direct involvement of oxygen adatoms (O^*) in C_3H_6 epoxidation, as proposed previously for $C_2H_4-O_2$ reactions from kinetic [19] and surface science [19,21] studies. In fact, DFT studies suggest that atomic oxygen inserts into the C=C bonds of adsorbed C_2H_4 [23] or C_3H_6 [24–27], forming oxametallacycle intermediates,

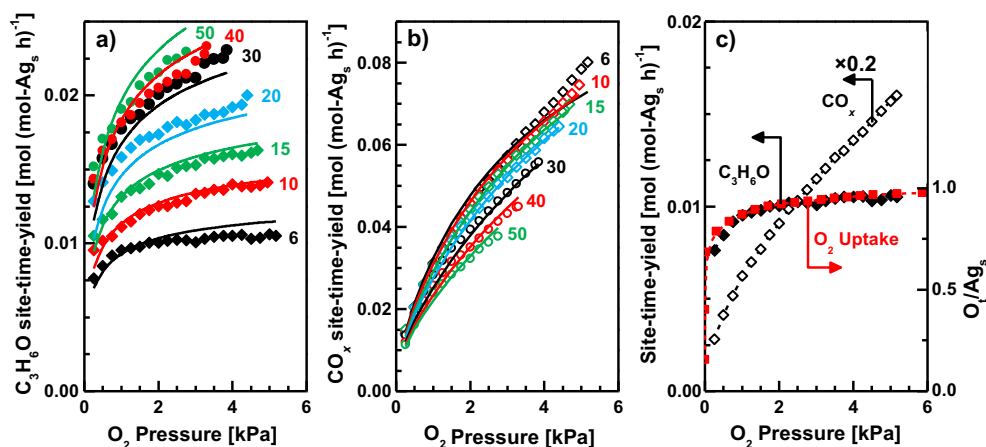


Fig. 4. Site-time-yields of (a) C_3H_6O ($\blacklozenge, \blacktriangle, \blackcircle, \blacksquare, \blacktriangleright, \blacklozenge, \blacktriangle, \blackcircle, \blacksquare, \blacktriangleright$) and (b) CO_x ($\diamond, \triangle, \circ, \square, \triangleright, \diamond, \triangle, \circ, \square, \triangleright$) during C_3H_6 - O_2 reactions on dispersed Ag clusters (5 wt% Ag/SiO₂, 5.1 nm clusters) as a function of O_2 pressures at 6 ($\blacklozenge, \blacktriangle, \blackcircle, \blacksquare, \blacktriangleright$), 10 ($\blacklozenge, \blacktriangle, \blackcircle, \blacksquare, \blacktriangleright$), 15 ($\blacklozenge, \blacktriangle, \blackcircle, \blacksquare, \blacktriangleright$), 20 ($\blacklozenge, \blacktriangle, \blackcircle, \blacksquare, \blacktriangleright$), 30 ($\blacklozenge, \blacktriangle, \blackcircle, \blacksquare, \blacktriangleright$), 40 ($\blacklozenge, \blacktriangle, \blackcircle, \blacksquare, \blacktriangleright$), and 50 ($\blacklozenge, \blacktriangle, \blackcircle, \blacksquare, \blacktriangleright$) kPa C_3H_6 at 443 K ($2 \times 10^3 \text{ cm}_3^{\text{STP}} \text{ g}_{\text{cat}}^{-1} \text{ h}^{-1}$). Predicted site-time-yields using Eqs. (4a) and (4b) and the kinetic and thermodynamic parameters in Table 1 (—). (c) Site-time-yields of C_3H_6O (\blacklozenge) and CO_x (\diamond) at 6 kPa C_3H_6 and equilibrium oxygen uptakes (O_i/Ag_s , \blacksquare) at 443 K plotted against O_2 pressures. The C_3H_6 reactant pressures are denoted in Fig. 4a and b.

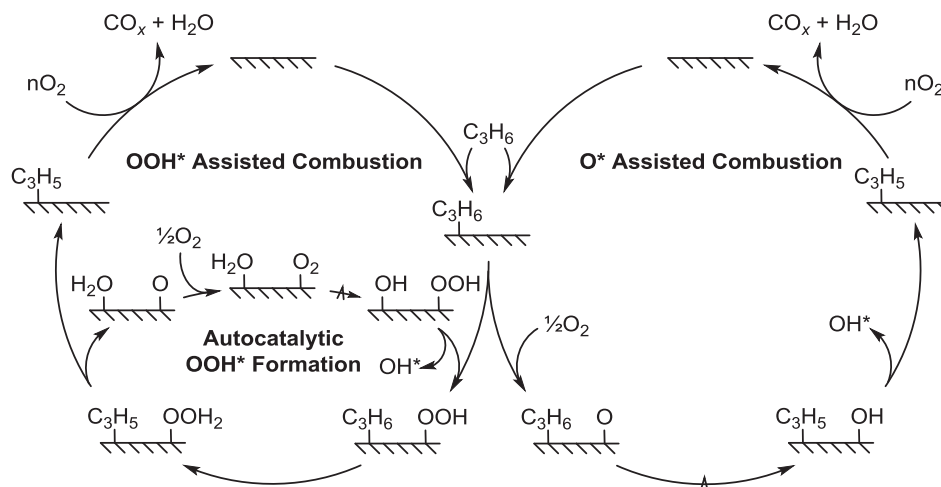
as the precursors to $C_nH_{2n}O$. At higher C_3H_6 pressures and larger $C_3H_6^*$ coverages (Fig. 3b), the profiles of C_3H_6O rate dependencies (Fig. 4a) appear to deviate from that of the equilibrium O^* contents (Fig. 4c), because $C_3H_6^*$ competitively adsorbs at and decreases the number of available Ag sites for O^* adsorption.

The C_3H_6O kinetic dependencies (Fig. 4a), the direct correlation between C_3H_6O site-time-yields and equilibrium O^* contents on surfaces largely free of $C_3H_6^*$ (Fig. 4c), and previous DFT studies [23–27] led us to propose that C_3H_6 epoxidation occurs via a series of elementary steps shown in Scheme 1. O_2 molecules may adsorb as diatomic (O_2^*) or monoatomic (O^*) species on Ag clusters [21,24,39,40,50–53] in quasi-equilibrated steps (Steps 1 and 2). Low energy electron diffraction (LEED) on Ag(1 1 1) [52] and Ag(1 1 0) [51] has detected these two discrete O_2^* and O^* adsorption configurations, isolated and identified with sequential temperature programmed desorption experiments [51,52]. Diatomic oxygen species prefer to bind in di- σ states, while oxygen adatoms settle in threefold fcc sites as their most stable adsorption configurations on Ag(1 1 1) surfaces [50]. Next, as shown in Scheme 1c, a $C_3H_6(g)$ molecule adsorbs at an Ag site (*) as $C_3H_6^*$ (Step 6) and then reacts with O^* in a quasi-equilibrated step to form the oxametallacycle (Ag-O-CH₂-CHCH₃-Ag, OMC, Step 7). Finally, the second C-O bond formation (Step 8) and the sequential desorption (Step 9) lead to C_3H_6O , completing the catalytic cycle.

In contrast to the C_3H_6O site-time-yields and O^* coverages, CO_x site-time-yields (r_{CO_x}) depend much more strongly on O_2 pressure (Fig. 4a–c). The r_{CO_x} values increase with O_2 pressures, even at the higher O_2 pressures (0.50–5.17 kPa) that lead to O^* coverages at near saturation (0.82–0.97 ML, Fig. 4c). Next, the rate dependence on O_2 at low C_3H_6 pressures does not resemble that of the equilibrium O^* coverages. These differences, taken together, suggest the involvement of a separate reactive oxygen species in CO_x formation than in C_3H_6 epoxidation. This oxygen species appears to form preferentially at higher O_2 pressures and high O^* coverages. At high O_2 pressures, small amounts of diatomic oxygen (O_2^*) tend to adsorb and remain on Ag surfaces, as predicted from the small equilibrium constant for O_2^* adsorption (K_{O_2}) of $3.4 \times 10^{-6} \text{ kPa}^{-1}$ at 443 kPa (estimation in Section S2). These O_2^* ($O^I O^{II}$) molecules may react with the H_2O^* , a product of combustion, and form $O^I O^{II}H^*$ through a H transfer step (Step 4), as proposed from DFT calculations on Ag(1 1 1) [54]. The $O^I O^{II}H^*$ molecules adsorb in bridge configurations at Ag sites through the O^I atom, according to DFT calculations on Ag(1 1 1) [50,54]. The parallel H transfer reaction from H_2O^* to O^* produces two OH^* species (Step 5).

We postulate that both the oxygen adatoms (O^*) and the hydroperoxyl species (OOH^*) act as effective H abstractors in C–H bond activation, a step in C_3H_6 combustion, according to Schemes 1d and 2. Later in Section 3.5, we probe and confirm the involvement of OOH^* as a more effective oxidant than O^* , O_2^* , and OH^* by comparing rates with C_3H_6 - O_2 , C_3H_6 - O_2 - H_2O , and C_3H_6 - O_2 - H_2O - H_2O_2 mixtures. The CO_x kinetic dependencies (Fig. 4b) are consistent with C_3H_6 combustion reactions that proceed via C–H bond cleavage by either O^* or OOH^* (Steps 10–11), the former involves the $C_3H_6^*O^*$ reaction and the latter involves the H transfer from H_2O^* to O_2^* as the kinetically relevant steps in Steps 10 and 4 of Scheme 1. At the entrance of the reactor, the O^* assisted C–H bond cleavage is the sole C_3H_6 combustion pathway since the H_2O pressure is zero. As the H_2O concentration increases along the reactor bed, the rates of autocatalytic OOH^* formation and OOH^* assisted C–H cleavage increase (Scheme 2).

The C_3H_6 combustion pathway begins with quasi-equilibrated C_3H_6 adsorption (Step 6), followed by $C_3H_6^*$ reactions with either O^* or OOH^* , undergoing C–H scission and forming an allyl intermediate ($C_3H_5^*$) along with OH^* or OOH_2^* in Steps 10 or 11, respectively. The sequential allyl oxidation and OOH_2^* decomposition steps lead to CO , CO_2 , and H_2O (Steps 12–15). The identity of the dominant kinetically relevant step proposed here for olefin combustion deviates from those derived from kinetic [14,18,19] and surface science [12,18,19,21] studies on Ag single crystals and polycrystalline surfaces, as well as from DFT calculations {Ag(1 0 0), Ag(1 1 1), and Al₂O₃ supported Ag₁₉ clusters} [24–27]. These previous studies suggest a kinetically relevant C–H bond activation step assisted solely by an atomic [21] or molecular [14] oxygen, but such proposals contradict the CO_x rate dependencies in Fig. 4b and their correlation to the O^* coverages in Fig. 4c. These previous studies, however, do agree with the fact that the C–H cleavage in $C_3H_6^*$ results in the formation of a surface allyl intermediate. We surmise that these mechanistic differences with respect to the kinetic relevance of steps that form CO_x between the literature and the proposed one in Scheme 1d are results of different reaction conditions and C_3H_6 conversion levels, as these factors alter the O_2^* and H_2O^* coverages and, in turn, the OOH^* formation rates. The previously reported rate dependencies [14] are consistent with the mechanistic route proposed in Schemes 1 and 2. We stress that, although the formation of OOH^* species remains undetected experimentally, likely because of their low concentrations, its formation as a stable adsorbate has been well-studied with DFT and their formation from the H_2O^* and O_2^* reaction is



Scheme 2. A proposed sequence of elementary steps for OOH* and O* assisted C₃H₆ combustion reactions on Ag clusters (–A→ denotes a rate determining step.)

favorable on Ag(111) surfaces [50,54] and Au₁₀ clusters on TiO₂(110) supports [55].

These elementary steps, the assumption of Langmuirian adsorption for O₂*, O*, H₂O*, and OH*, and the non-ideal C₃H₆ adsorption behavior captured by the Sips isotherm, lead to the following C₃H₆O (*r*_{C₃H₆O}) and CO_x (*r*_{CO_x}) site-time-yields, as derived in Section S5 of the Supplementary Information:

fractional coverages of 0.10–0.24, 0.0068–0.23, 3×10^{-4} – 1.8×10^{-2} , 3.4×10^{-4} – 2.2×10^{-3} , 5.6×10^{-7} – 1.3×10^{-5} , and 6.7×10^{-9} – 6.8×10^{-8} , respectively, during C₃H₆–O₂ catalysis. These results indicate that C₃H₆–O*, OH*, O₂*, and H₂O* coverages are insignificant. Omitting the terms associated with C₃H₆–O*, OH*, O₂*, and H₂O* in Eqs. (3a) and (3b) results in Eqs. (4a) and (4b):

$$r_{\text{C}_3\text{H}_6\text{O}} = \frac{k_{\text{C}_3\text{H}_6\text{O}^*} K_{\text{C}_3\text{H}_6} K_{\text{C}_3\text{H}_6\text{-O}^*} [\text{C}_3\text{H}_6]^\gamma K_{\text{O}_2}^{0.5} K_{\text{O}}^{0.5} [\text{O}_2]^{0.5}}{1 + K_{\text{O}_2}^{0.5} K_{\text{O}}^{0.5} [\text{O}_2]^{0.5} + K_{\text{C}_3\text{H}_6} [\text{C}_3\text{H}_6]^\gamma + K_{\text{O}_2}^{0.5} K_{\text{O}}^{0.5} K_{\text{C}_3\text{H}_6} K_{\text{C}_3\text{H}_6\text{-O}^*} [\text{O}_2]^{0.5} [\text{C}_3\text{H}_6]^\gamma + K_{\text{H}_2\text{O}}^{0.5} K_{\text{OH}}^{0.5} K_{\text{O}_2}^{0.25} K_{\text{O}}^{0.25} [\text{H}_2\text{O}]^{0.5} [\text{O}_2]^{0.25} + K_{\text{O}_2} [\text{O}_2] + K_{\text{H}_2\text{O}} [\text{H}_2\text{O}]}$$

$\uparrow \quad \uparrow \quad \uparrow \quad \uparrow \quad \uparrow \quad \uparrow \quad \uparrow$
 * O* C₃H₆* C₃H₆–O* OH* O₂* H₂O*

(3a)

$$r_{\text{CO}_x} = \frac{k_{\text{C}_3\text{H}_6\text{-O}^*} K_{\text{C}_3\text{H}_6} K_{\text{O}_2}^{0.5} K_{\text{O}}^{0.5} [\text{C}_3\text{H}_6]^\gamma [\text{O}_2]^{0.5} + k_{\text{OOH}} K_{\text{H}_2\text{O}} K_{\text{O}_2} [\text{H}_2\text{O}] [\text{O}_2]}{\left(1 + K_{\text{O}_2}^{0.5} K_{\text{O}}^{0.5} [\text{O}_2]^{0.5} + K_{\text{C}_3\text{H}_6} [\text{C}_3\text{H}_6]^\gamma + K_{\text{O}_2}^{0.5} K_{\text{O}}^{0.5} K_{\text{C}_3\text{H}_6} K_{\text{C}_3\text{H}_6\text{-O}^*} [\text{O}_2]^{0.5} [\text{C}_3\text{H}_6]^\gamma + K_{\text{H}_2\text{O}}^{0.5} K_{\text{OH}}^{0.5} K_{\text{O}_2}^{0.25} K_{\text{O}}^{0.25} [\text{H}_2\text{O}]^{0.5} [\text{O}_2]^{0.25} + K_{\text{O}_2} [\text{O}_2] + K_{\text{H}_2\text{O}} [\text{H}_2\text{O}]\right)^2}$$

$\uparrow \quad \uparrow \quad \uparrow \quad \uparrow \quad \uparrow \quad \uparrow \quad \uparrow$
 * O* C₃H₆* C₃H₆–O* OH* O₂* H₂O*

(3b)

where $k_{\text{C}_3\text{H}_6\text{O}^*}$, $k_{\text{C}_3\text{H}_6\text{-O}^*}$, and k_{OOH} are the rate constants for C₃H₆–O*, C₃H₆*–O*, and H₂O*–O₂* reactions, respectively; K_{O_2} , K_{O} , $K_{\text{C}_3\text{H}_6}$, $K_{\text{C}_3\text{H}_6\text{-O}^*}$, $K_{\text{H}_2\text{O}}$, and K_{OH} are the equilibrium constants for O₂ adsorption, O₂* dissociation, C₃H₆ adsorption on Ag (*), C₃H₆*–O* reactions, H₂O adsorption, and H₂O* dissociation, respectively, as defined in Scheme 1. The denominators of these rate equations give the relative abundances of the various surface species relative to the unoccupied sites (*) with their identities indicated underneath the respective terms. Adsorption enthalpies and entropies provide the estimated $K_{\text{O}_2} K_{\text{O}}$, $K_{\text{C}_3\text{H}_6}$, $K_{\text{C}_3\text{H}_6\text{-O}^*}$, $K_{\text{H}_2\text{O}} K_{\text{OH}}$, K_{O_2} , and $K_{\text{H}_2\text{O}}$ values of 4.7×10^{-2} , 6.8×10^{-3} , 3.2×10^{-3} , 1.6×10^{-3} , 3.4×10^{-6} , and 7.4×10^{-6} kPa^{–1}, respectively, at 443 K (calculations in Section S2). These values, together with the O₂, C₃H₆, and H₂O pressures (0.25–5.17 kPa O₂, 6–50 kPa C₃H₆, 0.0015–0.011 kPa H₂O), give O*, C₃H₆*, C₃H₆–O*, OH*, O₂*, and H₂O*

$$r_{\text{C}_3\text{H}_6\text{O}} = \frac{k_{\text{C}_3\text{H}_6\text{O}^*} K_{\text{C}_3\text{H}_6} K_{\text{C}_3\text{H}_6\text{-O}^*} [\text{C}_3\text{H}_6]^\gamma K_{\text{O}_2}^{0.5} K_{\text{O}}^{0.5} [\text{O}_2]^{0.5}}{1 + K_{\text{O}_2}^{0.5} K_{\text{O}}^{0.5} [\text{O}_2]^{0.5} + K_{\text{C}_3\text{H}_6} [\text{C}_3\text{H}_6]^\gamma}$$

$\uparrow \quad \uparrow \quad \uparrow$
 * O* C₃H₆*

(4a)

$$r_{\text{CO}_x} = \frac{k_{\text{C}_3\text{H}_6\text{-O}^*} K_{\text{C}_3\text{H}_6} K_{\text{O}_2}^{0.5} K_{\text{O}}^{0.5} [\text{C}_3\text{H}_6]^\gamma [\text{O}_2]^{0.5} + k_{\text{OOH}} K_{\text{H}_2\text{O}} K_{\text{O}_2} [\text{H}_2\text{O}] [\text{O}_2]}{\left(1 + K_{\text{O}_2}^{0.5} K_{\text{O}}^{0.5} [\text{O}_2]^{0.5} + K_{\text{C}_3\text{H}_6} [\text{C}_3\text{H}_6]^\gamma\right)^2}$$

$\uparrow \quad \uparrow \quad \uparrow$
 * O* C₃H₆*

(4b)

Table 1
Rate constant, equilibrium constant, and γ parameter values determined from non-linear regression of rate data measured during C_3H_6 - O_2 reactions (Fig. 4a and b) with the proposed rate equations (Eqs. (4a) and (4b)) on dispersed Ag clusters (5 wt% Ag/SiO₂, 5.1 nm clusters) at 443 K.

Parameter	$k_{C_3H_6O}K_{C_3H_6}K_{C_3H_6-O^*}$ [kPa ⁻¹ h ⁻¹]	$k_{C_3H_6-O^*}$ [h ⁻¹]	$k_{OOH}K_{H_2O}K_{O_2}$ [kPa ⁻² h ⁻¹]	$K_{O_2}K_O$ [kPa ⁻¹]	$K_{C_3H_6}$ [kPa ^{-0.40}]	γ
Value	$5.6 \times 10^{-3} \pm 0.2 \times 10^{-3}$	0.043 ± 0.003	$8.4 \times 10^2 \pm 1.0 \times 10^2$	19 ± 2	0.074 ± 0.013	0.40 ± 0.01

Eq. (4a) predicts that the reaction orders for C_3H_6O formation are positive and less than unity with O_2 and C_3H_6 ($0 \leq \alpha_{C_3H_6O} \leq 0.5$, $0 \leq \beta_{C_3H_6O} \leq \gamma$, where $0 \leq \gamma \leq 1$ is defined in Eq. (1)). Eq. (4b) predicts that the order for CO_x formation is less than unity with O_2 and positive or negative with C_3H_6 ($0 \leq \alpha_{CO_x} \leq 1$, $-2\gamma \leq \beta_{CO_x} \leq \gamma$, where $0 \leq \gamma \leq 1$). These predictions are consistent with the observed rate dependencies in Fig. 4a and b and with the calculated value of γ (0.78) from the equilibrium C_3H_6 uptakes in Fig. 3b.

These rate equations (Eqs. (4a) and (4b)) and the consideration of an integral plug flow reactor lead to a kinetic model that captures both the dependencies of C_3H_6O and CO_x site-time-yields. Non-linear regressions of all the rate data in Fig. 4a and b with the kinetic model give the values and standard deviations for the groupings of kinetic and thermodynamic parameters, $k_{C_3H_6O}K_{C_3H_6}K_{C_3H_6-O^*}$, $k_{C_3H_6-O^*}$, $k_{OOH}K_{H_2O}K_{O_2}$, $K_{O_2}K_O$, $K_{C_3H_6}$, and γ , as summarized in Table 1. Each parameter that appears in the numerator ($k_{C_3H_6O}K_{C_3H_6}K_{C_3H_6-O^*}$, $k_{C_3H_6-O^*}$, $k_{OOH}K_{H_2O}K_{O_2}$, $K_{O_2}K_O$, and γ) of Eqs. (4a) and (4b) has a standard error of less than 12% and is highly sensitive to the variation of its value. For example, a 20% change in their values increases the residual sum of squares between the predicted and measured site-time-yields by at least 250%, as demonstrated in Section S6 of the Supplementary Information. $K_{C_3H_6}$ appears only in the denominator and determines the small but not insignificant $C_3H_6^*$ coverages (0.01–0.10 ML). The $K_{C_3H_6}$ value has a standard error of 16% and is insensitive to perturbations: a 20% variation in the $K_{C_3H_6}$ value increases the residual sum of squared errors by at most 0.4%. Fig. 4a and b compares the measured and predicted site-time-yields and Fig. 5 shows the parity plot between them. The fraction of CO_x produced via the OOH^* assisted combustion pathway (Scheme 2) is between 0.71 and 0.95 under all inlet conditions. We also considered that the OOH^* formation does not occur ($k_{OOH} = 0$) and the O^* assisted combustion (Scheme 2) reaction is the only reaction that leads to CO_x

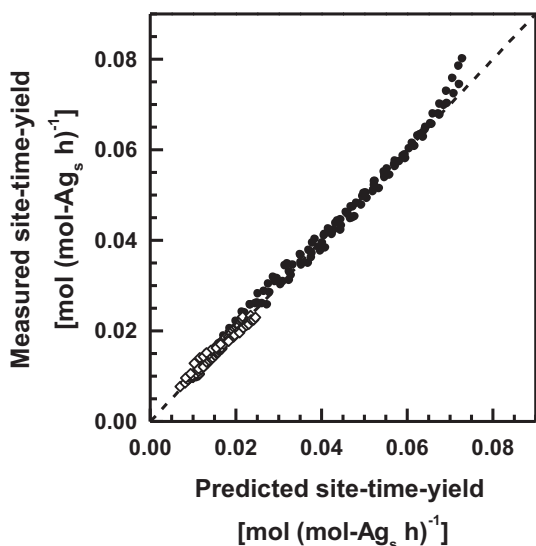


Fig. 5. Measured C_3H_6 (\diamond) and CO_x (\bullet) site-time-yields (per exposed Ag atom, 5 wt% Ag/SiO₂, 5.1 nm clusters) plotted against predicted site-time-yields from Eqs. (4a) and (4b) and parameters in Table 1 at 0.25–5.17 kPa O_2 and 6–50 kPa C_3H_6 (443 K, 2×10^3 cm_{STP} g_{cat}⁻¹ h⁻¹).

products, but such as a case cannot describe the observed CO_x rate dependencies, as shown in the poor parity plot in Fig. S4 of the Supplementary Information.

Next, we check the consistency of our model by comparing the thermodynamic values derived from the kinetic model (Table 1) to the reported values. The equilibrium constant for O_2 dissociation, $K_{O_2}K_O$, of 19 ± 2 kPa⁻¹, together with the entropy losses $\{-91$ J (mol O)⁻¹ K⁻¹, calculations in Section S2}, gives the average heat of O^* adsorption of 54 ± 1 kJ (mol O)⁻¹ during steady-state reactions at 0.62–0.90 ML O^* coverages, in agreement with those derived from equilibrium O_2 uptakes {Fig. 3a, 55 ± 1 kJ (mol O)⁻¹ for 0.16–0.99 ML O^* coverages}. We also compute the fractional O^* coverage during steady-state C_3H_6 - O_2 reactions:

$$\frac{[O^*]}{[Ag_s]} = \frac{K_{O_2}^{0.5} K_O^{0.5} [O_2]^{0.5}}{1 + K_{O_2}^{0.5} K_O^{0.5} [O_2]^{0.5} + K_{C_3H_6} [C_3H_6]^\gamma} \quad (5)$$

Eq. (5), together with the parameters in Table 1, gives the O^* coverages during steady-state C_3H_6 - O_2 reactions on 5.1 nm Ag clusters at 443 K. Fig. 3a compares these O^* coverages during steady-state reactions to the equilibrium O^* contents measured in the absence of C_3H_6 . O^* coverages during steady-state reactions are smaller than those at chemical equilibrium (without C_3H_6), simply because $C_3H_6^*$ species displace some of the O^* atoms. The O^* coverages increase sensitively with O_2 pressure but remain largely unperturbed by changing propylene pressure. Finally, we verify the O^* coverages independently by O_2 chemical titrations following the steady-state reactions (method and coverage calculations in Section S7). Table 2 compares the measured O^* coverages from O_2 chemical titrations and those calculated from Eq. (5) using the regressed parameters. These experimentally titrated O^* coverages coincide and correlate with those calculated from the proposed kinetic and thermodynamic coefficients.

On the other hand, the Sips isotherm parameter, γ , provides information about the nature of C_3H_6 adsorption during steady-state catalysis. The regressed γ value of 0.40 is smaller than that measured during equilibrium C_3H_6 uptakes (0.78, Fig. 3b, without O^*), indicating that C_3H_6 adsorption deviates from the Langmuirian behavior ($\gamma = 1$) to a much larger extent during steady-state reactions, during which surfaces remain largely covered with O^* , than those largely uncovered and contacted only to C_3H_6 . This difference reflects an increase in repulsive interactions between $C_3H_6^*$ and other adsorbates at high O^* coverages (0.62–0.90 ML) during reactions. Furthermore, the calculated fractional $C_3H_6^*$ coverages during steady-state C_3H_6 - O_2 reactions are:

Table 2
 O^* coverages (O^*/Ag_s) on dispersed Ag clusters (5 wt% Ag/SiO₂, 5.1 nm clusters) during steady-state C_3H_6 - O_2 reactions at 443 K predicted from Eq. (5) and measured with O_2 chemical titration after reactions.

Test	Reaction Conditions		Predicted O^*/Ag_s (Eq. (5))	Measured O^*/Ag_s with O_2 chemical titration
	O_2 [kPa]	C_3H_6 [kPa]		
1	0.25	50	0.62	0.48 ± 0.05
2	0.50	6	0.73	0.87 ± 0.02
3	1.75	30	0.82	0.84 ± 0.03
4	2.75	6	0.86	0.86 ± 0.03
5	3.30	40	0.86	0.88 ± 0.02
6	3.85	30	0.87	0.88 ± 0.04

$$\frac{[C_3H_6^*]}{[Ag_s]} = \frac{K_{C_3H_6}[C_3H_6]^7}{1 + K_{O_2}^{0.5}K_{O_2}^{0.5}[O_2]^{0.5} + K_{C_3H_6}[C_3H_6]^7} \quad (6)$$

As shown in Fig. 3b, the $C_3H_6^*$ coverages during the steady-state reactions remain smaller than equilibrium (without O_2), because of competitive O^* adatoms and the lateral repulsive interactions between O^* and $C_3H_6^*$, as captured by the Sips coefficient.

3.4. Reversibility of O_2 activation during C_3H_6 epoxidation inferred from the relative reactivities and kinetic dependencies during the oxidation of C_1 and C_3 oxygenates (methanol, acetone, and propylene oxide) and C_nH_{2n} olefins

We probe the reversibility of O_2 activation during C_3H_6 epoxidation, by comparing the magnitude and reaction orders for the net O_2 consumption rates with those during C_2H_4 , CH_3OH , C_3H_6 , and C_3H_6O (acetone and propylene oxide) oxidation. In general, the chemical equation for the reactions between O_2 and one of these reductants, R, leads to CO_2 , H_2O , and product P:



where v_j is the stoichiometric coefficients for species j . The net rates of oxygen consumption ($r_{O_2,R}$) relate to those of reductant R consumption (r_R) via the reaction stoichiometries $v_{O_2,R}$ and v_R :

$$r_{O_2,R} = \frac{v_{O_2,R}}{v_R} r_R = k_{eff,R} [O_2]^{\epsilon_R} [R]^{\phi_R} \quad (8)$$

where $k_{eff,R}$ is the effective rate constant for oxygen consumption, $[O_2]$ and $[R]$ are the oxygen and reductant pressures, and ϵ_R and ϕ_R are their reaction orders, respectively.

Table 3 summarizes the oxygen consumption rates and their rate dependencies for the various reductants R on Ag clusters at 443 K. Over 0.25–134 kPa O_2 , oxygen consumption rates for these reductants vary by five orders of magnitude $\{0.013\text{--}430 \text{ mol (mol-Ag}_s \text{ h)}^{-1}\}$. The largest oxygen consumption rates during CH_3OH oxidation (detailed results in Section S8) lead to rapid O^* scavenging from the Ag surfaces, thus reducing the O^* coverages to below equilibrium. For this reason, the reactivity is a single-valued function of the O_2/R ratio, as illustrated previously [56]. Similarly, the rate dependencies for C_2H_4 - O_2 reactions also vary with the operating O_2/R ratio (in Fig. S8) on 200 nm Ag clusters [57]. During CH_3OH and C_2H_4 oxidation at low O_2/R ratios, the apparent reaction orders with respect to O_2 and R are between 0.81 and 1 and between -0.31 and 0.19 , respectively [56–58]. These rate dependencies indicate that the kinetically relevant steps

for oxidation are O_2 activation on bare Ag sites (*). In both CH_3OH - O_2 and C_2H_4 - O_2 reactions, CH_3OH and C_2H_4 scavenge O^* adatoms effectively and decrease the O^* coverages to below equilibrium, and as a result, the O_2 activation step is irreversible.

Comparing the $r_{O_2,R}$ values in Table 3, the oxygen consumption rates during C_3H_6 , acetone, and propylene oxide oxidation are two to five orders of magnitude smaller than those during CH_3OH and C_2H_4 oxidation. These relative rate magnitudes confirm that $O_2(g)$ may dissociate and then recombine much more rapidly than the rate of O^* removal, as these reductants are less effective O^* scavengers than C_2H_4 and CH_3OH . We also measured the oxygen consumption rates during propylene, acetone, and propylene oxide combustion on 5.1 nm Ag clusters and report them in Fig. 6a and b as a function of O_2 and reductant pressures, respectively, at 443 K. The rate dependencies on O_2 are much smaller than unity (between 0.31 and 0.53, Table 3). These dependencies, taken together with the much smaller rates of $O_2(g)$ consumption than those during CH_3OH and C_2H_4 oxidation (r_{O_2,CH_3OH} , $r_{O_2,C_2H_4} \gg r_{O_2,C_3H_6}$, r_{O_2,C_3H_6O} (acetone), r_{O_2,C_3H_6O} (propylene oxide)), suggest that the O_2 dissociation step is kinetically-irrelevant during propylene, acetone, and propylene oxide oxidation and therefore must be quasi-equilibrated.

Despite their lower than first-order dependence on O_2 pressures, the oxygen consumption rates during C_3H_6 combustion and C_3H_6O (acetone and propylene oxide) oxidation remain insensitive to reductant pressures at 443 K, with β_{CO_x} , $\phi_{C_3H_6O}$ (acetone), and $\phi_{C_3H_6O}$ (propylene oxide) range between -0.10 and 0.04 (rate data in Fig. 4b and 6b). These dependencies suggest that the reductant activation step is also kinetically-irrelevant in propylene combustion and in acetone and propylene oxidation. The weak dependencies on O_2 pressure ($\alpha_{CO_x} = 0.55 \pm 0.05$) and the fact that Ag cluster surfaces remain covered predominantly with O^* indicate that the formation of another oxygen derived species such as OOH^* , rather than O^* , is the kinetically-relevant step for C_3H_6 combustion.

3.5. Catalytic effects of reactive oxygen species derived from O_2 , H_2O , and H_2O_2 oxidants on turnover rates and selectivities during C_3H_6 - O_2 reactions on Ag clusters

Here, we probe the potential catalytic involvement of four oxidant species, namely O^* , O_2^* , OH^* , and OOH^* , formed from the interconversion between O_2 and H_2O . Their coverages on Ag cluster surfaces and their catalytic roles in activating $C_yH_{2y-z}^*$ ($y = 1, 2$, or 3 and $z = 0, 1$, or 2) intermediates dictate the ultimate fate of C_3H_6 in epoxidation reactions.

Table 3

Oxygen consumption rates and kinetic dependencies during the reaction between R ($R = C_3H_6$, C_3H_6O (acetone or propylene oxide), C_2H_4 , or CH_3OH) and oxygen on Ag at 443 K.

Reductant (R)	Oxygen consumption turnover rate at 443 K ($r_{O_2,R}^a$) [mol (mol-Ag _s h) ⁻¹]	Apparent reaction order of O_2 (ϵ_R^a)	Apparent reaction order of R (ϕ_R^a)
$C_3H_6^b$	0.02–0.12 ^c	0.53 ± 0.10	-0.07 ± 0.05
C_3H_6O (acetone) ^b	0.025–0.036 ^d	0.31 ± 0.05	-0.03 ± 0.05
C_3H_6O (propylene oxide) ^b	0.013–0.035 ^e	0.36 ± 0.05	0.04 ± 0.05
$C_2H_4^f$	2–47 ^g	0.98 ± 0.03^g	-0.31 ± 0.03^g
		0.21 ± 0.04^h	1.00 ± 0.03^h
CH_3OH^b	40–430 ⁱ	0.49 ± 0.04	0.35 ± 0.04

^a $r_{O_2,R} = \frac{v_{O_2,R}}{v_R} r_R = k_{eff,R} [O_2]^{\epsilon_R} [R]^{\phi_R}$ (Eq. (8)).

^b 5 wt% Ag/SiO₂, 5.1 nm clusters.

^c 6–50 kPa C_3H_6 , 0.25–5.17 kPa O_2 , 443 K, $2 \times 10^3 \text{ cm}_3^3 \text{TP g}_{cat}^{-1} \text{ h}^{-1}$.

^d 0.093–0.25 kPa C_3H_6O (acetone), 1–3.5 kPa O_2 , 443 K, $2 \times 10^3 \text{ cm}_3^3 \text{TP g}_{cat}^{-1} \text{ h}^{-1}$.

^e 0.047–0.80 kPa C_3H_6O (propylene oxide), 0.25–3.5 kPa O_2 , 443 K, $2 \times 10^3 \text{ cm}_3^3 \text{TP g}_{cat}^{-1} \text{ h}^{-1}$.

^f Rate data from Ref. [57] are provided in Section S9. 8.1 wt% Ag/Al₂O₃, 200 nm clusters.

^g 7–134 kPa C_2H_4 , 6–53 kPa O_2 , $O_2/C_2H_4 < 1$, 493 K, $2.3 \times 10^3 \text{ cm}_3^3 \text{TP g}_{cat}^{-1} \text{ h}^{-1}$. Rate data from Ref. [57]. Rates measured under apparent O_2 reaction orders of 0.98 were extrapolated to 443 K using $E_a = 96 \text{ kJ mol}^{-1}$ [39].

^h 3–7 kPa C_2H_4 , 80–134 kPa O_2 , $O_2/C_2H_4 > 10$, 493 K, $2.3 \times 10^3 \text{ cm}_3^3 \text{TP g}_{cat}^{-1} \text{ h}^{-1}$. Rate data from Ref. [57].

ⁱ 1–4 kPa CH_3OH , 0.25–5 kPa O_2 , 443 K, $3 \times 10^5 \text{ cm}_3^3 \text{TP g}_{cat}^{-1} \text{ h}^{-1}$. Rate data are provided in Section S8.

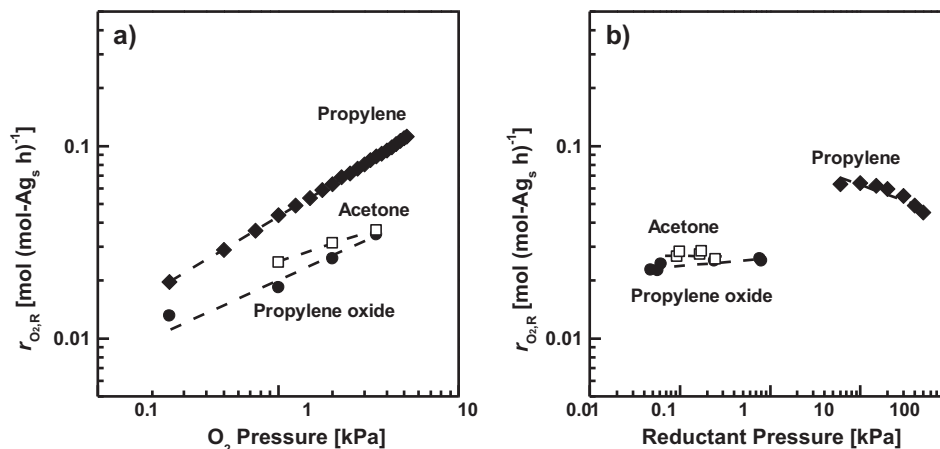


Fig. 6. Dependence of oxygen consumption turnover rates ($r_{O_2,R}$, per exposed Ag atom) during propylene (◆), acetone (□), and propylene oxide (●) combustion on (a) O₂ pressure (with 6 kPa propylene, 0.1 kPa acetone, or 0.85 kPa propylene oxide) and (b) reductant pressure (with 2 kPa O₂) on dispersed Ag clusters (5 wt% Ag/SiO₂, 5.1 nm clusters) at 443 K (2×10^3 cm³_{STP} g_{cat}⁻¹ h⁻¹).

O₂ adsorbs as O₂^{*} and O^{*} on Ag(1 1 1) [52] and Ag(1 0 0) [51], as detected by low-energy electron diffraction (LEED) spectra and isolated using temperature programmed experiments [51,52]. H₂O, a by-product from C₃H₆ combustion, may react with O^{*} to form OH^{*} or with O₂^{*} to form OOH^{*} and OH^{*} species. LEED spectra provide the evidence that OH^{*} forms on O^{*} covered Ag(1 1 0) [59] surfaces during H₂O adsorption, while DFT calculations demonstrate that OH^{*} and OOH^{*} exist as stable adsorbates on Ag(1 1 1) surfaces [50,54]. These H₂O derived species may act as oxidants during oxidation reactions. OOH^{*} provides a faster alternative pathway in CO oxidation, according to DFT calculations on Au₁₀ clusters on TiO₂ (1 1 0) [55]. In this pathway, the O^{II} atom of O^IO^{II}H^{*} acts as a nucleophile during its insertion into CO^{*} to form OCO^{II}H^{*}, which later decomposes into CO₂ [55]. This role of the O^{II} atom of O^IO^{II}H^{*} is similar to its involvement in C₃H₆ combustion, where it participates in the nucleophilic C-H bond cleavage of C₃H₆^{*} to form C₃H₅^{*} and H₂O^{II} (Steps 11–12, Scheme 1). Based on this knowledge, we propose that O^{*}, O₂^{*}, OH^{*}, and OOH^{*} oxidants may exist during C₃H₆-O₂ reactions, because H₂O is a side product.

Next, we probe the relative reactivities of O^{*}, O₂^{*}, OH^{*}, and OOH^{*} by examining C₃H₆ reactions with O₂, O₂-H₂O, or O₂-H₂O-H₂O₂ mixtures, because these mixtures lead to different O^{*}, O₂^{*}, OH^{*}, and OOH^{*} coverages. Fig. 7 shows the CO_x site-time-yields as a function of C₃H₆ pressure during C₃H₆ reactions with O₂, O₂-H₂O, and O₂-H₂O-H₂O₂ mixtures at 323 K. CO_x site-time-yields in C₃H₆-O₂ mixtures (2–50 kPa C₃H₆, 0.25 kPa O₂), which range from 5×10^{-4} to 8×10^{-4} mol (mol-Ag_s h)⁻¹, reflect the reactivity of O^{*} covered Ag clusters with small O₂^{*}, OH^{*}, and OOH^{*} coverages, because of the low H₂O pressures (10⁻⁴ kPa). CO_x site-time-yields with 2–50 kPa C₃H₆-0.25 kPa O₂-1.1 kPa H₂O mixtures are between 0.001 and 0.002 mol (mol-Ag_s h)⁻¹. These values are larger than those in C₃H₆-O₂ mixtures because of the larger H₂O pressure (1.1 kPa vs. 10⁻⁴ kPa in C₃H₆-O₂ mixtures) and the concomitant larger OH^{*} and OOH^{*} coverages. These higher rates with H₂O suggest that either OH^{*}, OOH^{*}, or both surface oxidants, promote C₃H₆ activation. Incorporating H₂O₂ into the feed (C₃H₆-O₂-H₂O-H₂O₂) increases the OOH^{*} coverages selectively, because H₂O₂ either dissociatively adsorbs as OOH^{*} and H^{*} or as two OH^{*} molecules, which recombine to form H₂O^{*} that transfers one of its hydrogen atoms to O₂^{*} to form OOH^{*}. The addition of 0.15 kPa H₂O₂ to the reaction mixtures and the higher OOH^{*} coverages increase in the CO_x site-time-yield by 2–20 folds, relative to those in C₃H₆-O₂ and C₃H₆-O₂-H₂O mixtures (Fig. 7). An increase in H₂O₂ pressure from 0.15 to 0.25 kPa causes a further CO_x site-time-yield

increase by another 1.2 to 2 times. These results suggest that OOH^{*} is a more effective oxidant than O^{*}, O₂^{*}, and OH^{*} for C₃H₆ activation.

Replacing the 1.1 kPa H₂O-0.15 kPa H₂O₂ reactants with partially deuterated compounds of 1.1 kPa H_mD_{2-m}O and 0.15 kPa H_pD_{2-p}O₂ ($m, p = 0, 1, \text{ or } 2$; 0.46 kPa H₂O, 0.51 kPa HDO, 0.13 kPa D₂O, 0.06 kPa H₂O₂, 0.07 kPa HDO₂, 0.02 kPa D₂O₂) decreases the site-time-yields by $17 \pm 2\%$ at >15 kPa C₃H₆ (Fig. 7). These isotopic effects, after considering the isotopic distributions of the deuterium atoms among the H_mD_{2-m}O and H_pD_{2-p}O₂, translate to a kinetic isotope effect for H₂O₂-to-D₂O₂ $\{(r_{CO_x, H_2O_2}) / (r_{CO_x, D_2O_2})\}^{-1}$ of 1.93 ± 0.12 . This kinetic isotope effect reflects the H₂O₂ or D₂O₂ dissociation (e.g., D₂O₂ → D^{*} + OOD^{*}) as a kinetically relevant step in C₃H₆ combustion. This strong kinetic isotope effect confirms that OOH^{*} or OOD^{*} directly involves in the kinetically relevant step

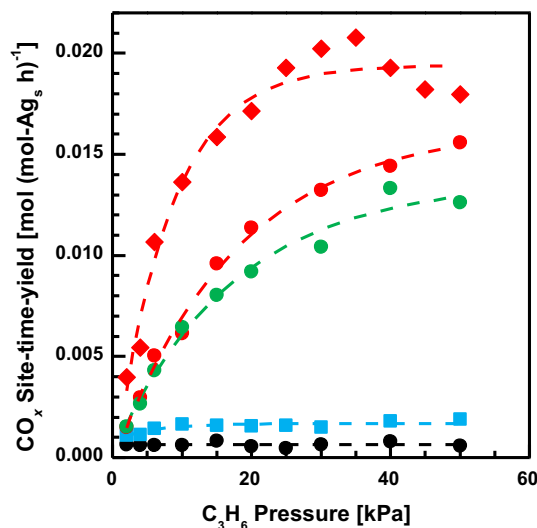


Fig. 7. CO_x site-time-yields (per exposed Ag atom) on dispersed Ag clusters (5 wt% Ag/SiO₂, 5.1 nm clusters) during C₃H₆ oxidation reactions in C₃H₆-O₂ mixtures with 0.25 kPa O₂ (●), in C₃H₆-O₂-H₂O mixtures with 0.25 kPa O₂ and 1.1 kPa H₂O (■), and in C₃H₆-O₂-H_mD_{2-m}O-H_pD_{2-p}O₂ ($m, p = 0, 1, \text{ or } 2$) mixtures with 0.25 kPa O₂, 1.1 kPa H_mD_{2-m}O (0.46 kPa H₂O, 0.51 kPa HDO, 0.13 kPa D₂O), and 0.15 kPa H_pD_{2-p}O₂ (0.06 kPa H₂O₂, 0.07 kPa HDO₂, 0.02 kPa D₂O₂) (●), 0.25 kPa O₂, 1.1 kPa H₂O, and 0.15 kPa H₂O₂ (●), and 0.25 kPa O₂, 1.1 kPa H₂O, and 0.25 kPa H₂O₂ (◆) as a function of C₃H₆ pressure at 323 K (2×10^3 cm³_{STP} g_{cat}⁻¹ h⁻¹).

for CO_x formation during C_3H_6 combustion in $\text{C}_3\text{H}_6\text{-O}_2\text{-H}_m\text{D}_{2-m}\text{O-H}_p\text{D}_{2-p}\text{O}_2$ mixtures.

We note that all reaction mixtures ($\text{C}_3\text{H}_6\text{-O}_2$, $\text{C}_3\text{H}_6\text{-O}_2\text{-H}_2\text{O}$, and $\text{C}_3\text{H}_6\text{-O}_2\text{-H}_m\text{D}_{2-m}\text{O-H}_p\text{D}_{2-p}\text{O}_2$) form CO_2 and H_2O as the predominant products while $\text{C}_3\text{H}_6\text{O}$ formation remains unobservable within the experimentally detectable limit (0.1 ppmv, which corresponds to a product selectivity smaller than 0.7%) at 323 K. The lack of $\text{C}_3\text{H}_6\text{O}$ formation on Ag, especially for the case with H_2O_2 oxidant, contradicts the high epoxidation selectivities ($\sim 90\%$) detected during $\text{C}_3\text{H}_6\text{-H}_2\text{O}_2$ reactions on homogeneous $\text{Mo}(\text{O})_2(\text{RO})_2$, $\text{VO}(\text{OOR})(\text{ROR})$, and $\text{Ti}(\text{OR})_4$ complexes (e.g., $\text{R} = \text{CH}_3$, CH_3CH_2) [2], as well as heterogeneous TiO_2 [7], titanium silicate (TS-1) [7], Ti-Beta [2], and Ti-MOR [2] catalysts. The contrasting selectivity indicates that the catalytic roles of OOH^* species differ between the two distinct classes of catalyst materials.

3.6. Effects of mean Ag cluster diameter and surface coordination on $\text{C}_3\text{H}_6\text{-O}_2$ turnover rates and selectivities

Here, we probe the effects of Ag cluster diameter, average surface Ag coordination, and their bindings to the adsorbates on the $\text{C}_3\text{H}_6\text{O}$ and CO_x site-time-yields (Eqs. (4a) and (4b)). Adsorption is less exothermic on (1 1 1) surfaces than the coordinatively less saturated (1 0 0) surfaces, edge sites, and corner sites, as predicted from the bond-order-bond-conservation principle [60] and confirmed with DFT calculations [24]. The heat of O^* adsorption is 61 kJ mol^{-1} on $\text{Ag}(111)$ and it increases to 92 kJ mol^{-1} on $\text{Ag}(100)$, when both surfaces contain 0.22 ML O^* [24].

Fig. 8 shows $\text{C}_3\text{H}_6\text{O}$ and CO_x site-time-yields ($r_{\text{C}_3\text{H}_6\text{O}}$ and r_{CO_x}) as a function of mean cluster diameter (3.1–29.3 nm Ag, 1 and 5 wt% Ag/ SiO_2) during $\text{C}_3\text{H}_6\text{-O}_2$ reactions (3 kPa O_2 , 10 kPa C_3H_6) at 443 K. Increasing the mean Ag cluster diameter leads to a commensurate increase in the $\text{C}_3\text{H}_6\text{O}$ site-time-yield by a factor of ~ 4.8 . As the mean Ag cluster diameter increases, the average coordination of exposed Ag atoms increases, and thus, the average heat of O^* adsorption decreases and the equilibrium constant for O^* adsorption ($K_{\text{O}_2}K_{\text{O}}$, Steps 1–2) becomes smaller. This decrease in the $K_{\text{O}_2}K_{\text{O}}$ term affects both the numerator and denominator of the $\text{C}_3\text{H}_6\text{O}$ site-time-yield equation (Eq. (4a)), because the denominator term $K_{\text{O}_2}^{0.5}K_{\text{O}}^{0.5}[\text{O}_2]^{0.5}$ is the dominant term and O^* is the most abundant surface intermediate (0.62–0.90 ML O^*), as shown in

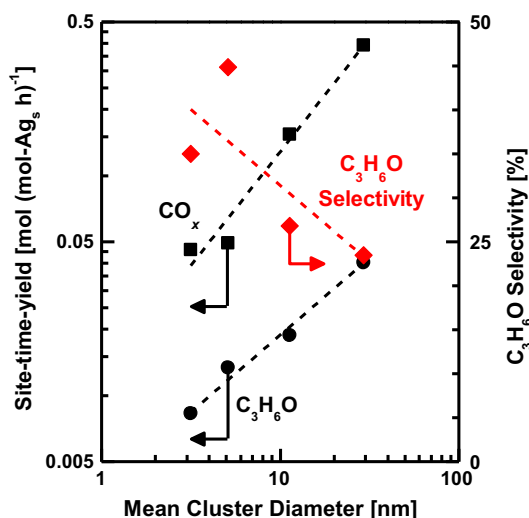


Fig. 8. Site-time-yields of $\text{C}_3\text{H}_6\text{O}$ (●) and CO_x (■) and $\text{C}_3\text{H}_6\text{O}$ selectivities (◆) during $\text{C}_3\text{H}_6\text{-O}_2$ reactions on dispersed Ag clusters (1 and 5 wt% Ag/ SiO_2) as a function of their mean cluster diameters (determined by O_2 chemisorption) at 443 K (3 kPa O_2 , 10 kPa C_3H_6 , $2 \times 10^3 \text{ cm}^3_{\text{TP}} \text{ g}_{\text{cat}}^{-1} \text{ h}^{-1}$).

Section 3.3. Thus, the net cluster size effects on the site-time-yields of $\text{C}_3\text{H}_6\text{O}$ (Eq. (4a)) primarily reflect the increase in the rate constant, $k_{\text{C}_3\text{H}_6\text{O}^*}$ (Step 8), as the O^* atoms become more weakly bound on the larger Ag clusters, thus decreasing the activation barriers for C_3H_6 epoxidation reactions.

The site-time-yield for CO_x formation increases more sensitively with cluster diameter than that for $\text{C}_3\text{H}_6\text{O}$ formation, i.e., by a factor of ~ 8.5 as cluster diameter increases from 3.1 to 29.3 nm (Fig. 8). As a result of this increase, the selectivity to $\text{C}_3\text{H}_6\text{O}$ decreases by a factor of ~ 1.5 . As cluster diameter increases, the heats of O_2^* , O^* , C_3H_6^* , and H_2O^* adsorption and the related equilibrium constants K_{O_2} , $K_{\text{O}_2}K_{\text{O}}$, $K_{\text{C}_3\text{H}_6}$, and $K_{\text{H}_2\text{O}}$ decrease. The more weakly bound C_3H_6^* , O^* , H_2O^* , and O_2^* reactants on the larger clusters may also decrease the energy difference between the reactant and the transition state for $\text{C}_3\text{H}_6\text{-O}^*$ combustion and OOH^* formation reactions, thus decreasing the activation barriers and increasing the $k_{\text{C}_3\text{H}_6\text{-O}^*}$ and k_{OOH} values. In combination, these changes in the rate and equilibrium constants ($k_{\text{C}_3\text{H}_6\text{-O}^*}$, k_{OOH} , K_{O_2} , $K_{\text{O}_2}K_{\text{O}}$, $K_{\text{C}_3\text{H}_6}$, and $K_{\text{H}_2\text{O}}$) explain the net cluster size effects on the CO_x site-time-yields (Eq. (4b)). The changes in the numerator $K_{\text{O}_2}K_{\text{O}}$, $K_{\text{C}_3\text{H}_6}$, K_{O_2} , and $K_{\text{H}_2\text{O}}$ terms are partially compensated by the changes of the dominant $K_{\text{O}_2}K_{\text{O}}$ term in the denominator of Eq. (4b). Therefore, the effects of cluster size on CO_x site-time-yields reflect predominantly the net increases in $k_{\text{C}_3\text{H}_6\text{-O}^*}$ and k_{OOH} with increasing coordinative saturation of the Ag sites.

4. Conclusions

Rate measurements in the kinetically controlled regime, together with oxygen and propylene uptakes, lead to a proposed sequence of elementary steps that describes the concomitant propylene epoxidation and combustion reactions on dispersed Ag clusters. C_3H_6 reacts with an adsorbed oxygen adatom (O^*) to produce the desired propylene oxide. In the parallel C_3H_6 combustion sequence, the kinetically relevant step does not involve C_3H_6 and O_2 activation. We hypothesize that hydrogen transfer from physisorbed H_2O^* , a product of the combustion reaction, to O_2^* leads to the formation of a hydroperoxyl intermediate (OOH^*) that participates in the hydrogen abstraction from C_3H_6^* as a route to CO , CO_2 , and H_2O formation. Rates measured with $\text{C}_3\text{H}_6\text{-O}_2\text{-H}_2\text{O-H}_2\text{O}_2$ mixtures suggest the catalytic involvements of the hydroperoxyl species, as these mixtures lead to larger OOH^* surface contents, more effective hydrogen abstraction, and in turn, higher C_3H_6 combustion rates, as also confirmed from strong $\text{H}_2\text{O}_2/\text{D}_2\text{O}_2$ kinetic isotope effects. Kinetic analyses of both the $\text{C}_3\text{H}_6\text{O}$ and CO_x formation rates show that Ag cluster surfaces are predominantly covered with O^* adatoms and a small fraction of C_3H_6^* . O_2 adsorption and activation remain quasi-equilibrated because the rates of O^* scavenging by C_3H_6 are small and insignificant relative to the much larger rates of O_2 dissociation and O^* recombination. C_3H_6 adsorption is quasi-equilibrated and exhibits non-ideal behavior captured by the Sips isotherm, which accounts for the variation in the heat of C_3H_6^* adsorption with an exponential distribution. Larger Ag clusters bind O^* , O_2^* , C_3H_6^* , and H_2O^* more weakly than smaller clusters and promote both CO_x much more than $\text{C}_3\text{H}_6\text{O}$ formation, therefore, the selectivities towards $\text{C}_3\text{H}_6\text{O}$ decrease.

Acknowledgements

This study was supported by the Natural Sciences and Engineering Research Council of Canada and the Canada Foundation for Innovation. We also acknowledge the Queen Elizabeth II Graduate Scholarships in Science & Technology and the Ontario Graduate Scholarships awarded to Petar T. Lachkov.

Appendix A. Supplementary material

Supplementary data associated with this article can be found in the online version, at <https://doi.org/10.1016/j.jcat.2018.07.011>.

References

- [1] T.A. Nijhuis, M. Makkee, J.A. Moulijn, B.M. Weckhuysen, *Ind. Eng. Chem. Res.* 45 (2006) 3447–3459.
- [2] S.T. Oyama, in: *Mech. Homog. Heterog. Epoxidation Catal.*, Elsevier, Amsterdam, 2008, pp. 3–99.
- [3] D.L. Trent, *Kirk-Othmer Encycl. Chem. Technol.*, John Wiley & Sons, Inc., 2001.
- [4] W.F. Richey, *Kirk-Othmer Encycl. Chem. Technol.*, John Wiley & Sons, Inc., 2000.
- [5] J.K.F. Buijink, J.-P. Lange, A.N.R. Bos, A.D. Horton, F.G.M. Niele, in: *Mech. Homog. Heterog. Epoxidation Catal.*, Elsevier, 2008, pp. 355–371.
- [6] K.-T. Li, C.-C. Lin, P.-H. Lin, in: *Mech. Homog. Heterog. Epoxidation Catal.*, Elsevier, 2008, pp. 373–386.
- [7] M. Haruta, J. Kawahara, in: *Mech. Homog. Heterog. Epoxidation Catal.*, Elsevier, 2008, pp. 297–313.
- [8] T.A. Nijhuis, E. Sacaliuc, B.M. Weckhuysen, in: *Mech. Homog. Heterog. Epoxidation Catal.*, Elsevier, 2008, pp. 339–354.
- [9] A.M. Joshi, B. Taylor, L. Cumarantunge, K.T. Thomson, W. Nicholas Delgass, in: *Mech. Homog. Heterog. Epoxidation Catal.*, Elsevier, 2008, pp. 315–338.
- [10] S. Linic, M.A. Barteau, *J. Catal.* 214 (2003) 200–212.
- [11] C. Stegelmann, N.C. Schiødt, C.T. Campbell, P. Stoltze, *J. Catal.* 221 (2004) 630–649.
- [12] P.A. Kilty, W.M.H. Sachtler, *Catal. Rev.* 10 (1974) 1–16.
- [13] J. Lu, J.J. Bravo-Suárez, A. Takahashi, M. Haruta, S. Oyama, *J. Catal.* 232 (2005) 85–95.
- [14] N.W. Cant, W.K. Hall, *J. Catal.* 52 (1978) 81–94.
- [15] R.A. Van Santen, C.P.M. de Groot, *J. Catal.* 98 (1986) 530–539.
- [16] W. Yao, G. Lu, Y. Guo, Y. Guo, Y. Wang, Z. Zhang, *J. Mol. Catal. Chem.* 276 (2007) 162–167.
- [17] S.R. Seyedmonir, J.K. Plischke, M.A. Vannice, H.W. Young, *J. Catal.* 123 (1990) 534–549.
- [18] C.T. Campbell, *J. Catal.* 94 (1985) 436–444.
- [19] R.B. Grant, R.M. Lambert, *Surf. Sci.* 146 (1984) 256–268.
- [20] A. Ayame, S. Eimaeda, L. Feng, H. Hayasaka, *Appl. Catal. Gen.* 304 (2006) 93–108.
- [21] E.A. Carter, W.A. Goddard III, *J. Catal.* 112 (1988) 80–92.
- [22] C. Stegelmann, P. Stoltze, *J. Catal.* 226 (2004) 129–137.
- [23] S. Linic, M.A. Barteau, *J. Am. Chem. Soc.* 124 (2002) 310–317.
- [24] A. Pulido, P. Concepción, M. Boronat, A. Corma, *J. Catal.* 292 (2012) 138–147.
- [25] D. Torres, N. Lopez, F. Illas, R.M. Lambert, *Angew. Chem.* 119 (2007) 2101–2104.
- [26] L.M. Molina, S. Lee, K. Sell, G. Barcaro, A. Fortunelli, B. Lee, S. Seifert, R.E. Winans, J.W. Elam, M.J. Pellin, *Catal. Today* 160 (2011) 116–130.
- [27] L. Cheng, C. Yin, F. Mehmood, B. Liu, J. Greeley, S. Lee, B. Lee, S. Seifert, R.E. Winans, D. Teschner, R. Schlögl, S. Vajda, L.A. Curtiss, *ACS Catal.* 4 (2014) 32–39.
- [28] M. García-Diéguez, Y.-H. (Cathy) Chin, E. Iglesia, *J. Catal.* 285 (2012) 260–272.
- [29] S.J. Blanksby, G.B. Ellison, *Acc. Chem. Res.* 36 (2003) 255–263.
- [30] J. Huang, M. Haruta, *Res. Chem. Intermed.* 38 (2012) 1–24.
- [31] W. Su, S. Wang, P. Ying, Z. Feng, C. Li, *J. Catal.* 268 (2009) 165–174.
- [32] W. Song, D.M. Perez Ferrandez, L. van Haandel, P. Liu, T.A. Nijhuis, E.J.M. Hensen, *ACS Catal.* 5 (2015) 1100–1111.
- [33] S. Kanungo, Y. Su, M.F.N. d'Angelo, J.C. Schouten, E.J.M. Hensen, *Catal. Sci. Technol.* 7 (2017) 2252–2261.
- [34] X. Zheng, Q. Zhang, Y. Guo, W. Zhan, Y. Guo, Y. Wang, G. Lu, *J. Mol. Catal. Chem.* 357 (2012) 106–111.
- [35] Z. Song, N. Mimura, J.J. Bravo-Suárez, T. Akita, S. Tsubota, S.T. Oyama, *Appl. Catal. Gen.* 316 (2007) 142–151.
- [36] H. Chu, L. Yang, Q. Zhang, Y. Wang, *J. Catal.* 241 (2006) 225–228.
- [37] S.J. Khatib, S.T. Oyama, *Catal. Rev.* 57 (2015) 306–344.
- [38] G. Bergeret, P. Gallezot, in: *Handb. Heterog. Catal.*, Wiley-VCH, Weinheim, 2008, pp. 738–765.
- [39] A.W. Czanderna, *J. Phys. Chem.* 68 (1964) 2765–2771.
- [40] W.W. Smeltzer, E.L. Tollefson, A. Cambron, *Can. J. Chem.* 34 (1956) 1046–1060.
- [41] D.R. Lide, *CRC Handbook of Chemistry and Physics*, 78th ed., CRC Press, Boca Raton, Florida, 1997.
- [42] J.J.F. Scholten, J.A. Konvalinka, F.W. Beekman, *J. Catal.* 28 (1973) 209–220.
- [43] A.F. Benton, L.C. Drake, *J. Am. Chem. Soc.* 56 (1934) 255–263.
- [44] S. Chrétien, M.S. Gordon, H. Metiu, *J. Chem. Phys.* 121 (2004) 9931–9937.
- [45] I. Langmuir, *J. Am. Chem. Soc.* 40 (1918) 1361–1403.
- [46] M.I. Temkin, V. Pyzhev, *Acta Physiochim. USSR* 12 (1940) 217–222.
- [47] R. Sips, *J. Chem. Phys.* 16 (1948) 490–495.
- [48] I. Onal, D. Düzenli, A. Seubsai, M. Kahn, E. Seker, S. Senkan, *Top. Catal.* 53 (2009) 92–99.
- [49] J. Lu, J.J. Bravo-Suárez, M. Haruta, S.T. Oyama, *Appl. Catal. Gen.* 302 (2006) 283–295.
- [50] D.C. Ford, *Surf. Sci.* 604 (2010) 1565–1575.
- [51] M.A. Barteau, R.J. Madix, *Surf. Sci.* 97 (1980) 101–110.
- [52] C.T. Campbell, *Surf. Sci.* 157 (1985) 43–60.
- [53] K. Prince, G. Paolucci, A. Bradshaw, K. Horn, C. Mariani, *Vacuum* 33 (1983) 867.
- [54] W.-S. Sheu, M.-W. Chang, *Surf. Sci.* 628 (2014) 104–110.
- [55] J. Saavedra, H.A. Doan, C.J. Pursell, L.C. Grabow, B.D. Chandler, *Science* 345 (2014) 1599–1602.
- [56] W. Tu, Y.-H. (Cathy) Chin, *Angew. Chem. Int. Ed.* 53 (2014) 12148–12152.
- [57] P.D. Klugherz, P. Harriott, *AIChE J.* 17 (1971) 856–866.
- [58] R.E. Kenson, M. Lapkin, *J. Phys. Chem.* 74 (1970) 1493–1502.
- [59] E.M. Stuve, R.J. Madix, B.A. Sexton, *Surf. Sci.* 111 (1981) 11–25.
- [60] E. Shustorovich, in: *Adv. Catal.*, Academic Press, 1990, pp. 101–163.